Electronic Supporting Information

Facile methyl group transfer from Pt^{II} to gallium and indium

R. Govindarajan,[a] Pavan K. Vardhanapu,[a] Robert R. Fayzullin,[b] Eugene Khaskin,[a] and Julia R. Khusnutdinova *[a]

Table of Contents

General specifications

If not indicated otherwise, all reactions were performed using standard Schlenk or glovebox techniques under a dry argon atmosphere. Unless noted otherwise, all chemicals were purchased from major commercial suppliers (TCI, Sigma-Aldrich, and Nacalai Tesque) and used without purification. Anhydrous solvents were dispensed from an MBRAUN solvent purification system and degassed before use. Anhydrous deuterated solvents were purchased from Eurisotop and stored over 4 Å molecular sieves. The ligand **L** and complex **1** were prepared according to the previously reported procedure.[1] All the metal complexes were synthesized under an argon atmosphere in a glove box.

NMR spectra were measured on JEOL ECZ600R 600 MHz, and Bruker Avance III Neo 500 MHz (CryoProbe) spectrometers. The following abbreviations are used for describing NMR spectra: s (singlet), d (doublet), t (triplet), br (broad); Pt satellites are marked with a star in the figures showing NMR spectra. Electrospray Ionization Mass Spectrometry (ESI-MS) measurements were performed on a Thermo Scientific LTQ-Orbitrap apparatus and Mass Spectrometer Bruker timsTOF LC/IMS-Q-TOF. FT-IR spectra were measured using Agilent Cary 630 with an ATR module in an argon-filled glovebox. The following abbreviations are used for describing FT-IR spectra: s (strong), m (medium), w (weak), br (broad). Absorbance UV/vis spectra were collected using an Agilent Cary 60 instrument. The elemental analysis was not performed due to the high reactivity of the complexes in the presence of trace moisture introduced during sample storage and analysis. The purity was assessed based on multinuclear NMR.

Synthesis and characterization

Synthesis of [(L)GaClPtMe][GaMeCl$_3$], 2

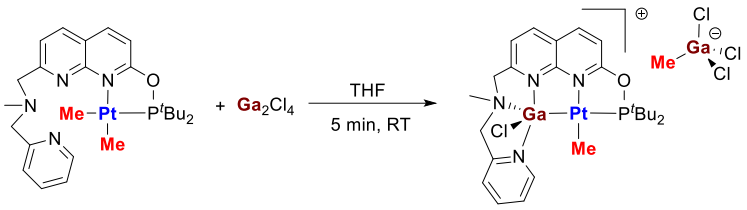

Scheme S1. Formation of **2**.

In Ar filled glovebox, complex **1** (26 mg, 0.04 mmol), Ga_2Cl_4 (11 mg, 0.04 mmol) were placed in a 5 mL vial. To the solid mixture 2 mL of dry THF was added and the mixture was left stirring for 5 min at room temperature (RT). The solvent was evaporated under vacuum and the remaining yellow solid was washed with 2 mL of pentane, obtaining pure complex **2**, in 89% yield (33 mg). The crystals of complex **2** were obtained by dissolving **2** in dichloromethane and diffusing the solution with pentane.

^{1}H NMR (600 MHz, CD_2Cl_2) δ 9.07 (d, *J* = 5.4 Hz, 1H, CH_{Naph}), 8.65 (d, *J* = 8.9 Hz, 1H, CH_{Naph}), 8.57 (d, *J* = 7.1 Hz, 1H, CH_{Naph}), 8.08 (t, *J* = 7.6 Hz, 1H, CH_{Py}), 7.72 (d, *J* = 7.8 Hz, 1H, CH_{Py}), 7.66 (d, *J* = 7.8 Hz, 1H, CH_{Py}), 7.62 (m, 2H, CH_{Naph} & CH_{Py}), 4.94 (d, *J* = 15.9 Hz, 1H, CH_2), 4.79 (d, *J* = 15.0 Hz, 1H, CH_2), 4.57 (d, *J* = 16.1 Hz, 1H, CH_2), 4.41 (d, *J* = 15.0 Hz, 1H, CH_2), 2.54 (s, 3H, N-CH_3), 1.73 (d, $^3J_{PH}$= 7.2 Hz, $^2J_{PtH}$ = 88.3, 3H, Pt-Me), 1.54 (d, *J* = 15.0 Hz, 9H, $C(CH_3)_3$), 1.39 (d, *J* = 14.7 Hz, 9H, $C(CH_3)_3$), 0.18 (s, 3H, Ga-Me).

^{13}C{^{1}H} NMR (151 MHz, CD_2Cl_2) δ 167.80 (Cq, $_{Naph}$), 156.06 (Cq, $_{Naph}$), 151.76 (Cq, $_{Py}$), 149.56 ($C_{H,\ Naph}$), 146.55 (Cq, $_{Naph}$), 142.37 ($C_{H,\ Naph}$), 141.91 ($C_{H,\ Naph}$), 141.26 ($C_{H,\ Py}$), 125.36 ($C_{H,\ Py}$), 124.50 ($C_{H,\ Py}$), 120.87 ($C_{H,\ Py}$), 120.41(Cq, $_{Naph}$), 115.16 ($C_{H,\ Naph}$), 62.15 (CH_2), 60.61(CH_2), 42.95 (N-CH_3), 42.45 (C(***C***$H_3)_3$), 41.75 (d, *J* = 7.8 Hz, ***C***$(CH_3)_3$), 27.58 (dd, *J* = 15.3, 7.0 Hz, C(***C***$H_3)_3$), -3.73 (Ga-Me), -33.94 ($^1J_{PtC}$ = 634.07 Hz, Pt-Me).

^{31}P{^{1}H} NMR (243 MHz, CD_2Cl_2, 25 °C) δ: 191.1 ($^1J_{PtP}$ = 2291 Hz).

ESI-HRMS (m/z pos): Found (Calcd):

$[(L)PtMeGaCl]^+[CH_3GaCl_3]^-$,$C_{25}H_{36}O_1N_4P^{195}PtCl^{69}Ga^+$: 738.1151 (738.1213).

ESI-HRMS (m/z neg): Found (Calcd): $[(L)PtMeGaCl]^{+}[CH_3GaCl_3]^{-}$, $CH_3Cl_3{}^{69}Ga^{-}$: 190.8631 (190.8535).

FT-IR (ATR, solid): 2947 (br, m), 2868 (br, m), 1605 (s), 1560 (w), 1513 (m), 1437 (s), 1368 (m), 1332 (s), 1255 (w), 1183 (m),1138 (m), 1059 (s), 1014 (s), 862 (s), 809 (s), 762 (s), 729 (m), 691 (w) cm^{-1}.

UV-vis (THF), λ, nm (ε, $M^{-1}\cdot cm^{-1}$) : 221 (30005), 262 (16036), 316 (6524), 328 (6424).

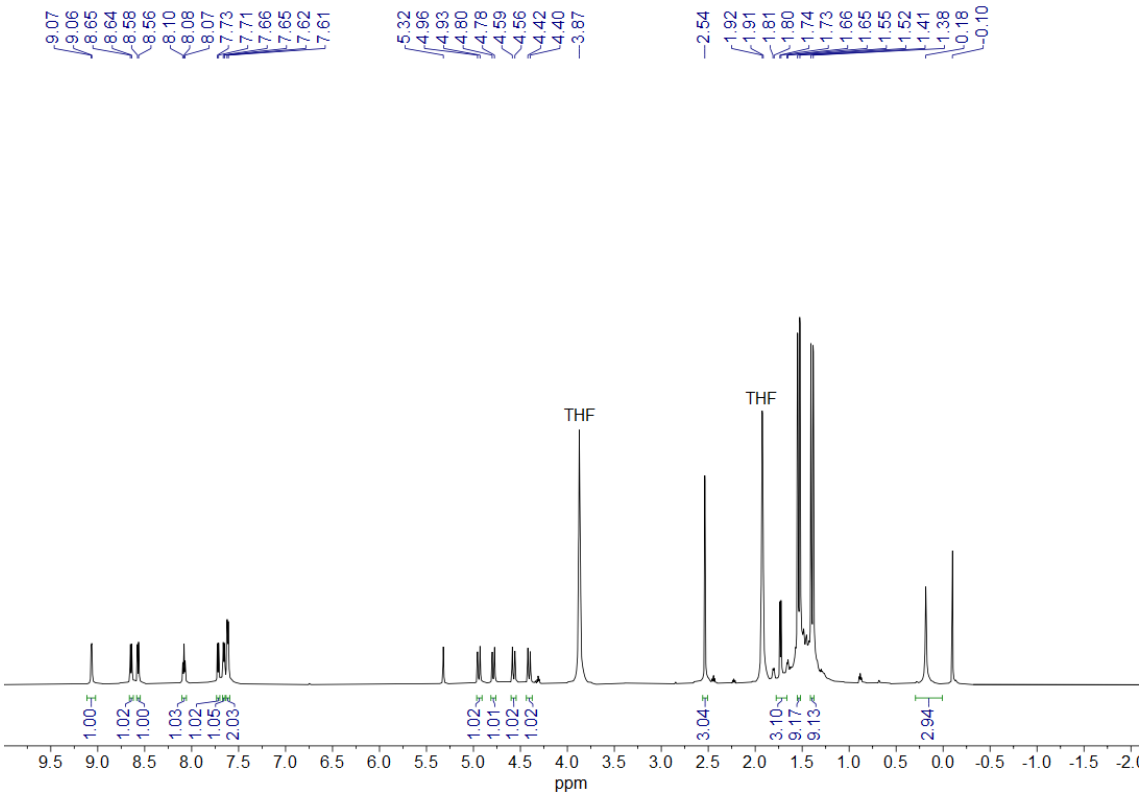

Figure S1. ^{1}H NMR spectrum of **2** in CD_2Cl_2 at 25 °C.

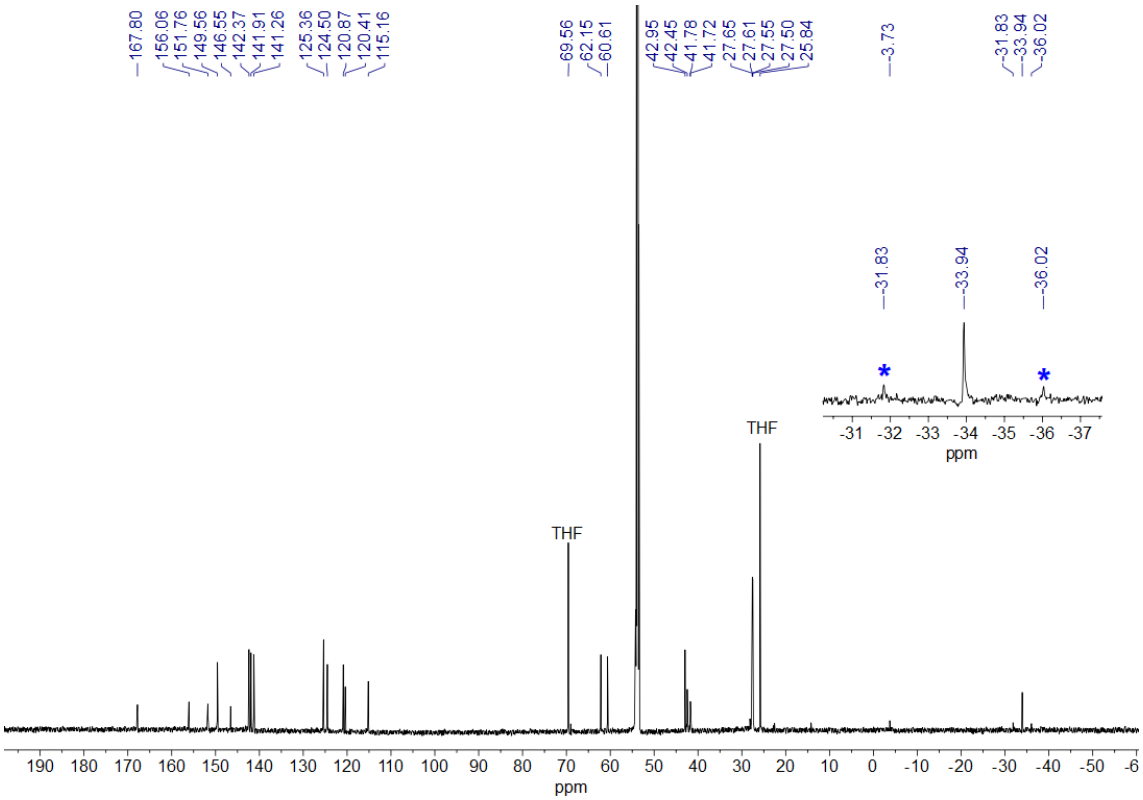

Figure S2. $^{13}C\{^{1}H\}$ NMR spectrum of **2** in CD_2Cl_2 at 25 °C. Pt satellites is marked with stars.

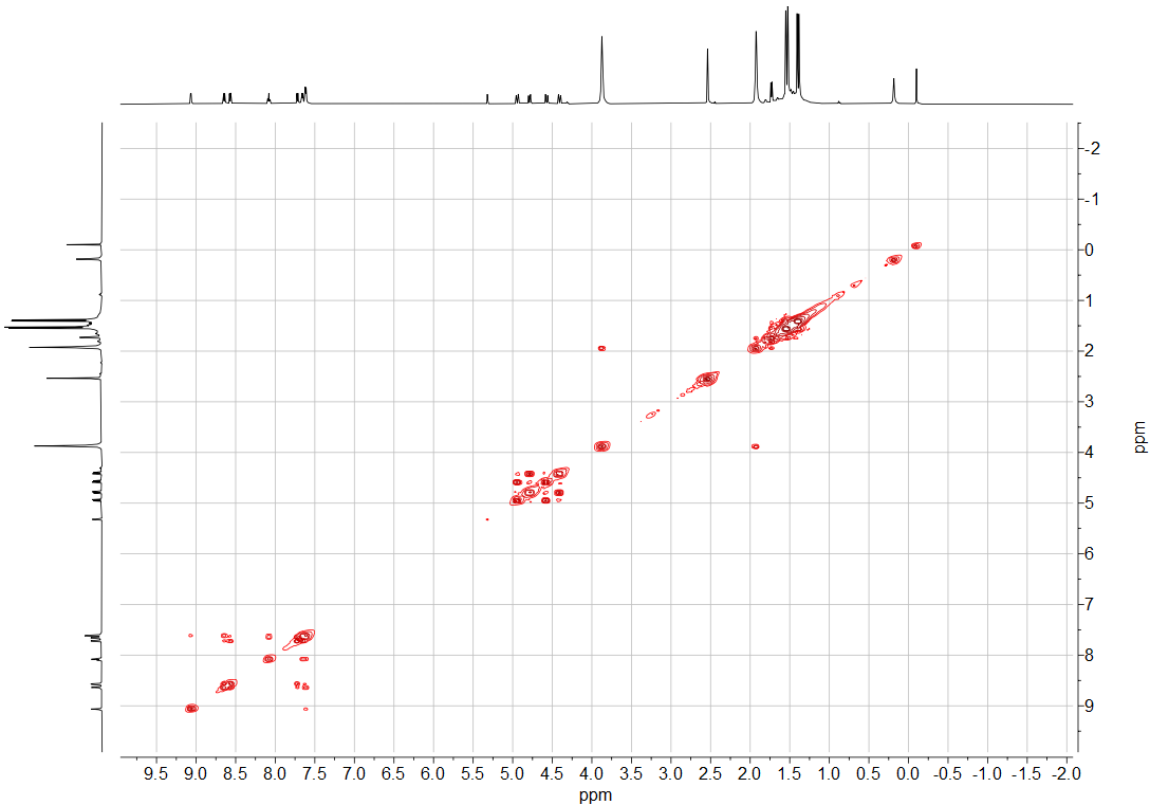

Figure S3. ^{1}H-^{1}H COSY spectrum of **2** in CD_2Cl_2 at 25 °C.

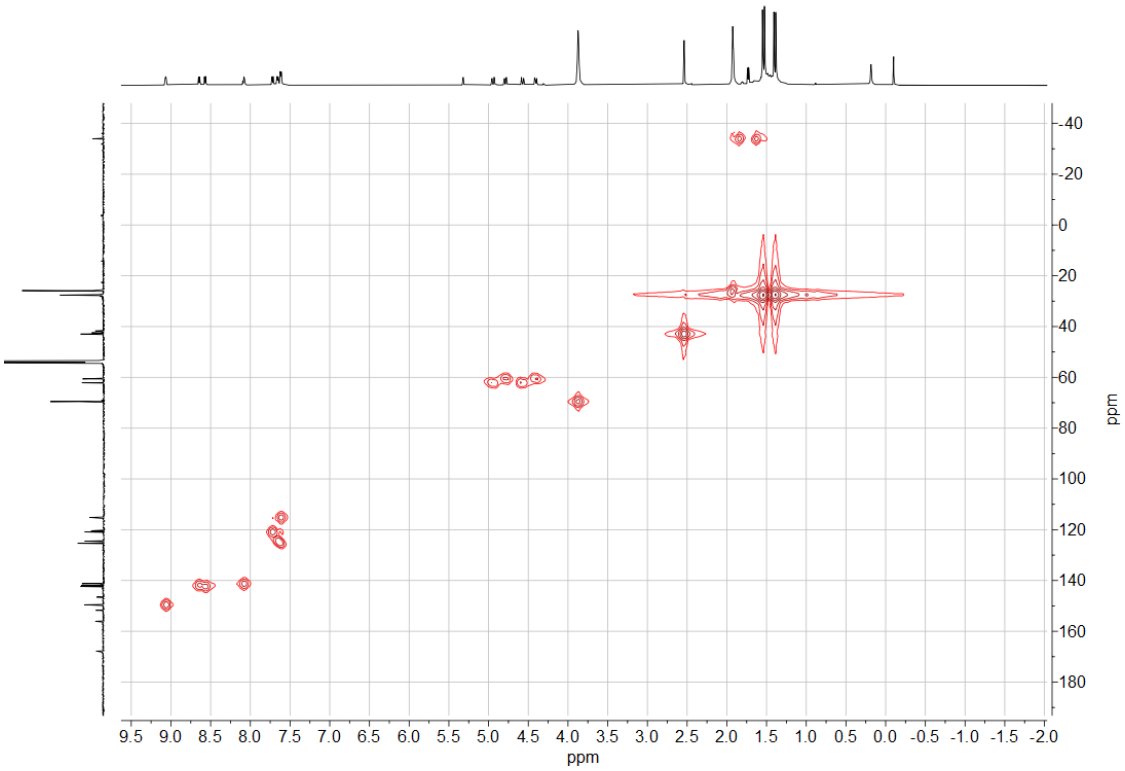

Figure S4. ^{1}H-^{13}C HMQC spectrum of **2** in CD_2Cl_2 at 25 °C.

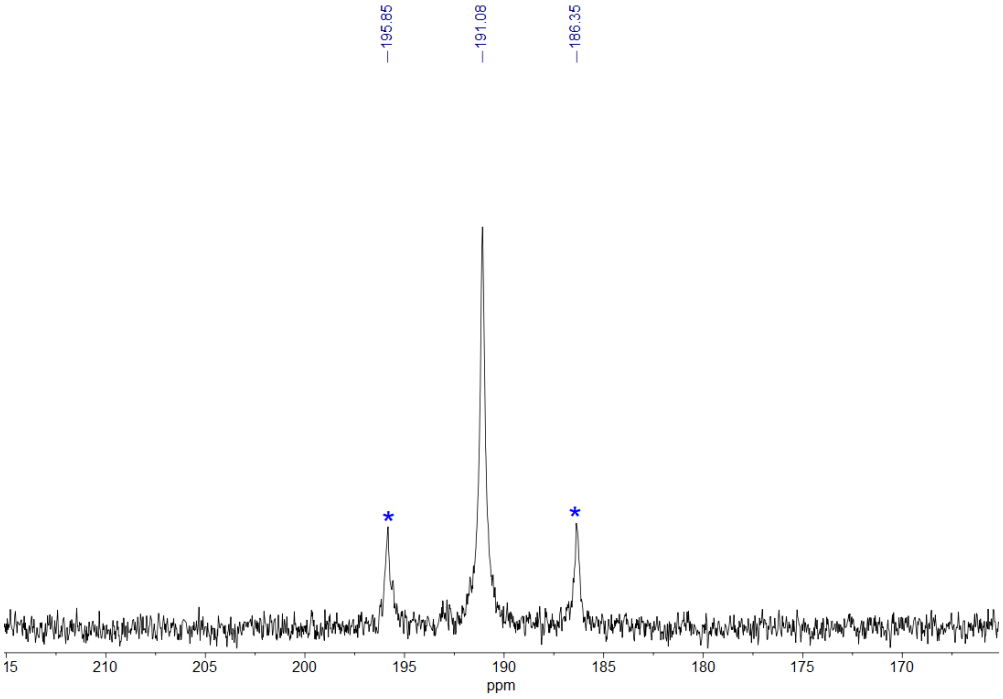

Figure S5. $^{31}P\{^{1}H\}$ NMR spectrum of **2** in THF-d_8 at 25 °C. Pt satellites are marked with stars.

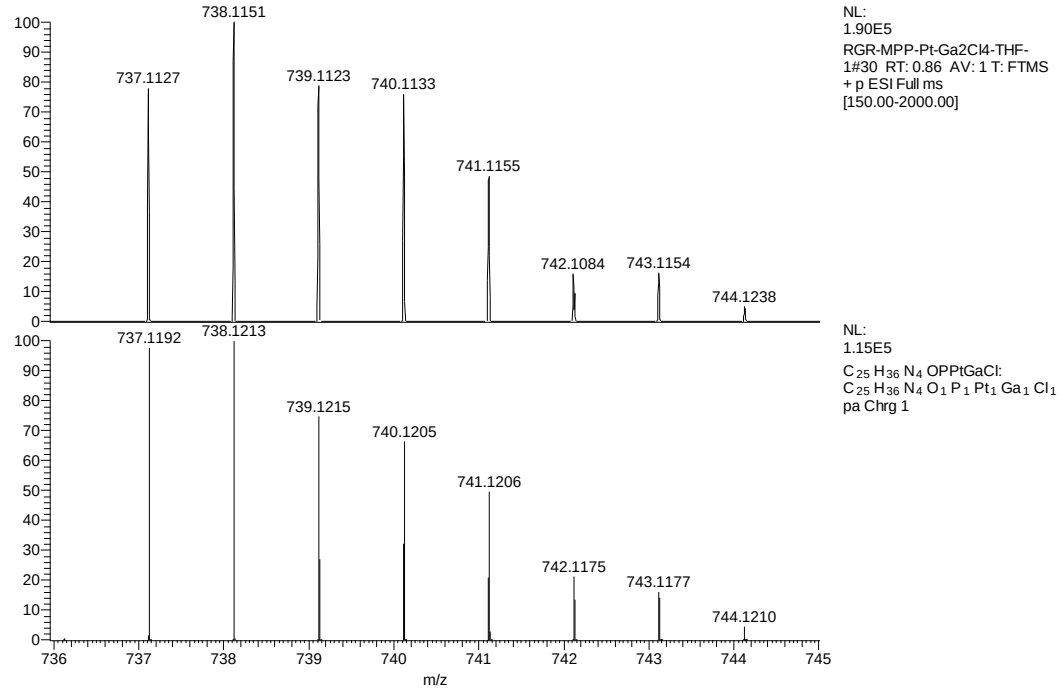

Figure S6. Positive mode ESI-(HR)MS of a THF solution of **2** (top) and simulated spectrum for $[(L)PtMeGaCl]^+[CH_3GaCl_3]^-$, $C_{25}H_{36}O_1N_4P^{195}PtCl^{69}Ga^+$ (bottom).

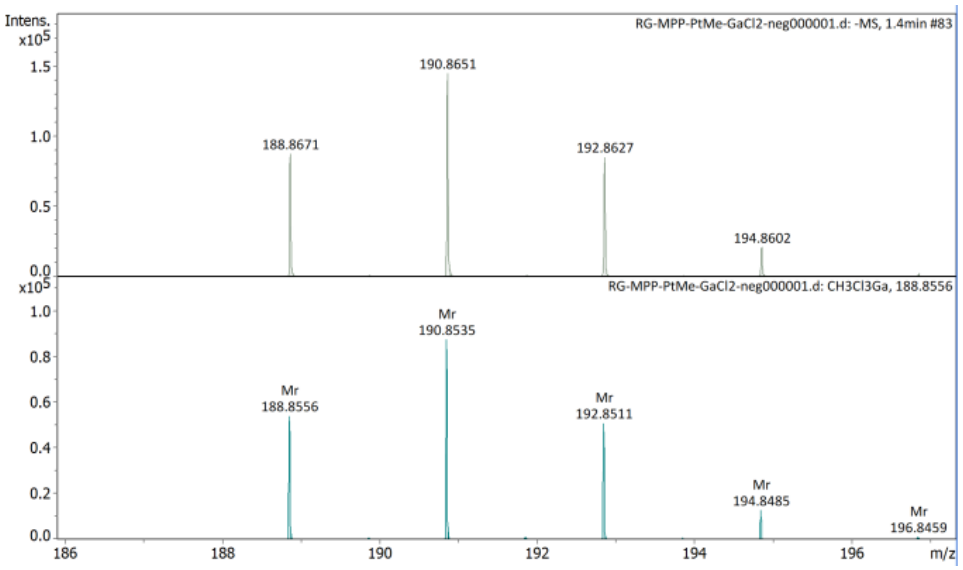

Figure S7. Negative mode ESI-(HR)MS of a acetonitrile solution of **2** (top) and simulated spectrum for $[(L)PtMeGaCl]^+[CH_3GaCl_3]^-$, $CH_3Cl_3{}^{69}Ga^-$ (bottom).

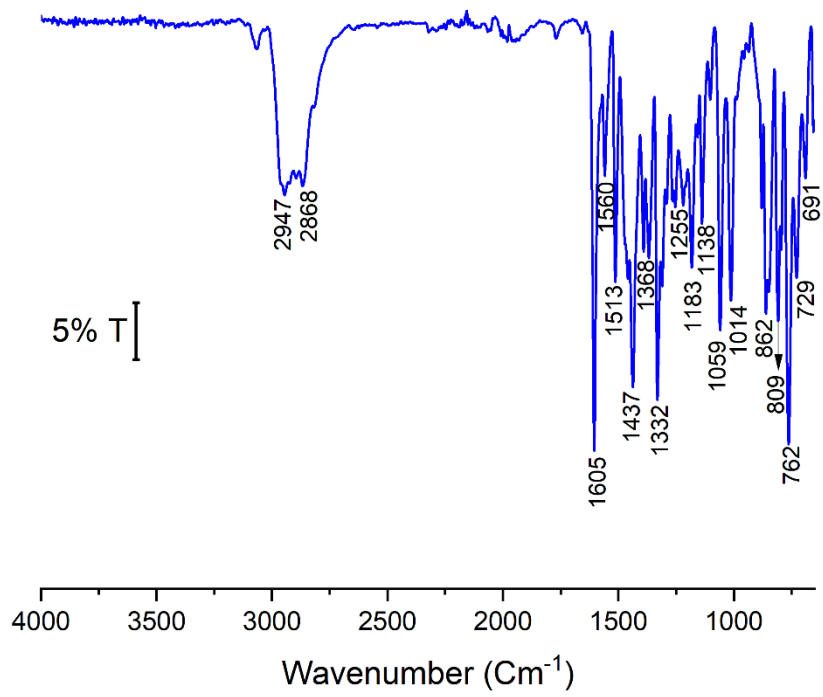

Figure S8. ATR FT-IR transmittance spectrum of **2**.

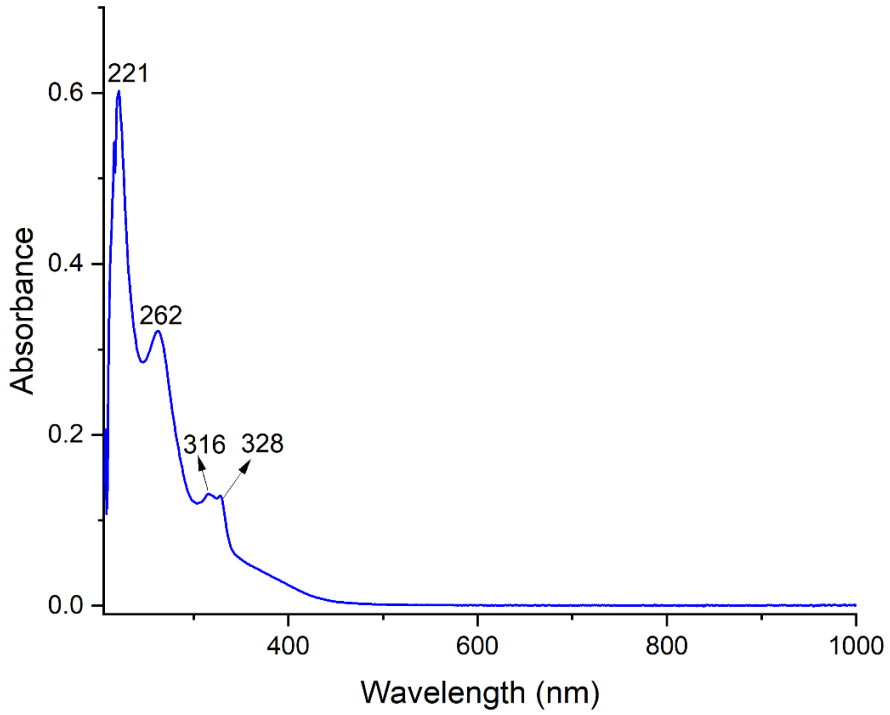

Figure S9. UV-vis absorbance spectrum for **2** (20.1 x 10^{-6} M) in THF.

NMR monitoring of the formation of 2 in situ

To a solution of **1** (6.5 mg, 0.01 mmol) in THF-d_8 (0.5 mL) in a J. Young NMR tube, Ga_2Cl_4 (3 mg, 0.01 mmol) was added, and the reaction was monitored with ^{1}H NMR spectrum, which showed the clean formation of $GaCH_3$ after 5 minutes.

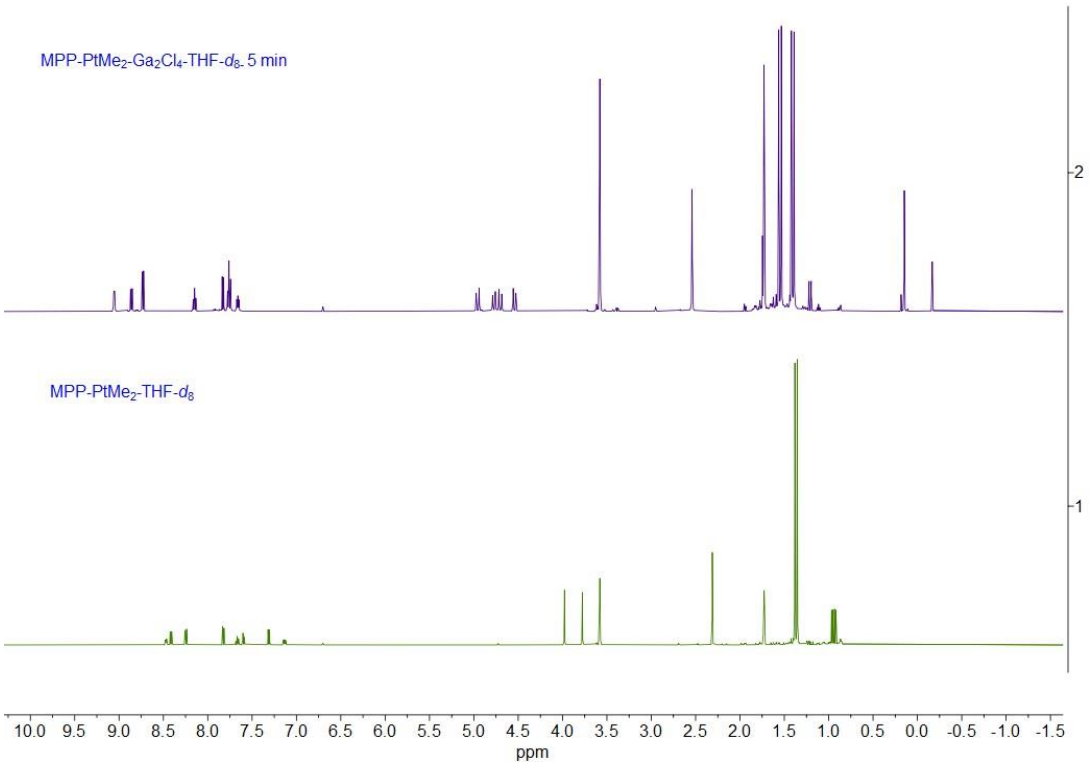

Figure S10. Full ^{1}H NMR spectrum of **1** (bottom) and **1** after reaction with Ga_2Cl_4 for 5 min (top) in THF-d_8 at 25 °C.

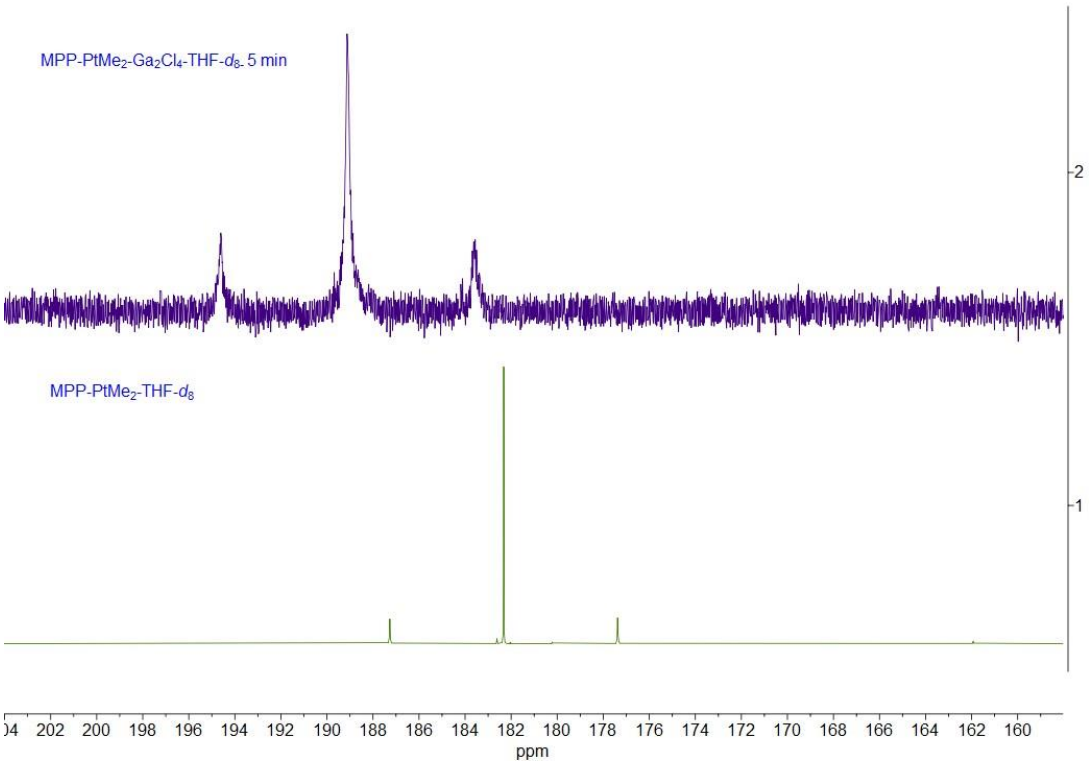

Figure S11. Full $^{31}P\{^{1}H\}$ NMR spectrum of **1** (bottom) and **1** after reaction with Ga_2Cl_4 for 5 min (top) in THF-d_8 at 25 °C.

Synthesis of [(L)InClPtMe][InMeCl$_3$], 3

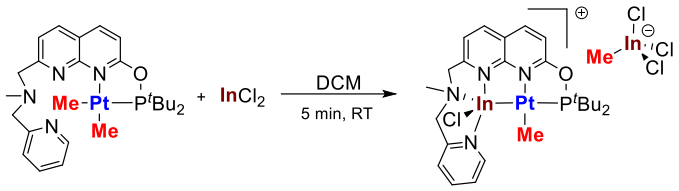

Scheme S2. Formation of **3**.

In Ar filled glovebox, complex **1** (39 mg, 0.06 mmol), $InCl_2$ (26 mg, 0.14 mmol) were placed in a 20 mL vial. To the solid mixture 5 mL of dichloromethane was added and the mixture was left stirring for 5 min at room temperature (RT). The reaction mixture was filtered through celite then evaporated under vacuum and the remaining yellow solid was washed with 5 mL of diethyl ether, obtaining pure complex **3**. The crystals of complex **3** were obtained by dissolving the complex in dichloromethane and diffusing with diethyl ether to get pure orangish yellow crystals in 90% yield (55 mg).

^{1}H NMR (600 MHz, CD_2Cl_2, 20 °C) δ 8.83 (d, *J* = 5.3 Hz, 1H, CH_{Naph}), 8.68 (d, *J* = 8.6 Hz, 1H, CH_{Naph}), 8.60 (d, *J* = 8.2 Hz, 1H, CH_{Naph}), 8.09 (t, *J* = 7.6 Hz, 1H, CH_{Py}), 7.78 (d, *J* = 8.4 Hz, 1H, CH_{Naph}), 7.67 (d, *J* = 7.8 Hz, 1H, CH_{Py}), 7.63 (m, 2H, CH_{Py}), 5.02 (d, *J* = 15.6 Hz, 1H, CH_2), 4.94 (d, *J* = 15.2 Hz, 1H, CH_2), 4.53 (d, *J* = 15.6 Hz, 1H, CH_2), 4.31 (d, *J* = 14.4 Hz, 1H, CH_2), 2.39 (s, 3H, N-CH_3), 1.88 (d, $^3J_{PH}$ = 7.4 Hz, 3H, Pt-Me), 1.53 (d, *J* = 15.2 Hz, 9H, $C(CH_3)_3$), 1.42 (d, *J* = 15.1 Hz, 9H, $C(CH_3)_3$), 0.18 (s, 3H, In-Me).

^{13}C{^{1}H} NMR (151 MHz, CD_2Cl_2, 20 °C) δ 168.04 (Cq, $_{Naph}$), 158.13 (Cq, $_{Naph}$), 153.41(Cq, $_{Py}$), 150.06 (C_H, $_{Naph}$), 147.73 (Cq, $_{Naph}$), 142.95 (C_H, $_{Naph}$), 142.72 (C_H, $_{Naph}$), 141.53 (C_H, $_{Py}$), 125.92 (C_H, $_{Py}$), 125.52 (C_H, $_{Py}$), 122.01(C_H, $_{Naph}$), 120.98 (Cq, $_{Naph}$), 114.97 (C_H, $_{Py}$), 61.55 (CH_2), 60.51 (CH_2), 42.78 (d, *J* = 5.6 Hz, (***C***$(CH_3)_3$), 42.35 (N-CH_3), 42.13 (d, *J* = 8.3 Hz, (***C***$(CH_3)_3$), 27.63 (dd, *J* = 22.3, 6.1 Hz, C(***C***$H_3)_3$), -2.92 (In-CH_3), -40.23 (Pt-Me).

^{31}P{^{1}H} NMR (243 MHz, CD_2Cl_2, 20 °C) δ: 183.7 (br, $^2J_{PtP}$ ~ 2800 Hz).

ESI-HRMS (m/z pos): Found (Calcd): $[(L)PtMeInCl]^+[CH_3InCl_3]^-$,

$C_{25}H_{36}O_1N_4P^{195}PtCl^{115}In^+$: 784.1054 (784.0999).

ESI-HRMS (m/z neg): Found (Calcd): $[(L)PtMeInCl]^{+}[CH_3InCl_3]^{-}$, $CH_3Cl_3{}^{115}In^{-}$: 234.8523 (234.8338).

FT-IR (ATR, solid): 3065 (br, w), 2957 (br, w), 2870 (br, w), 1604 (s), 1554 (m), 1514 (s), 1458 (m), 1429 (s), 1368 (m), 1324 (s), 1266 (m), 1246 (m), 1217 (m), 1183 (m),1126 (m), 1053 (s), 1015 (s), 863 (s), 809 (s), 772 (s), 731 (s), 701 (w) cm^{-1}.

UV-vis (CH_2Cl_2), λ, nm (ε, $M^{-1}\cdot cm^{-1}$) : 278 (37304), 314 (12399), 329 (11045).

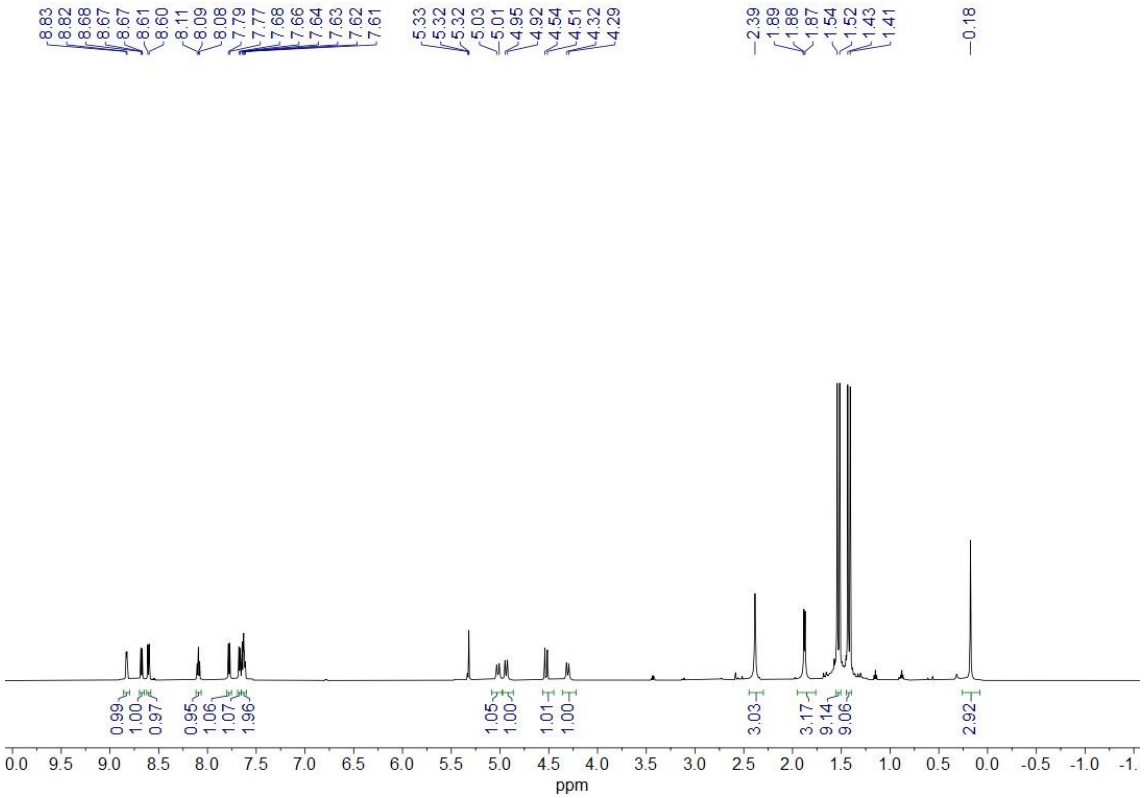

Figure S12. ^{1}H NMR spectrum of **3** in CD_2Cl_2 at 25 °C.

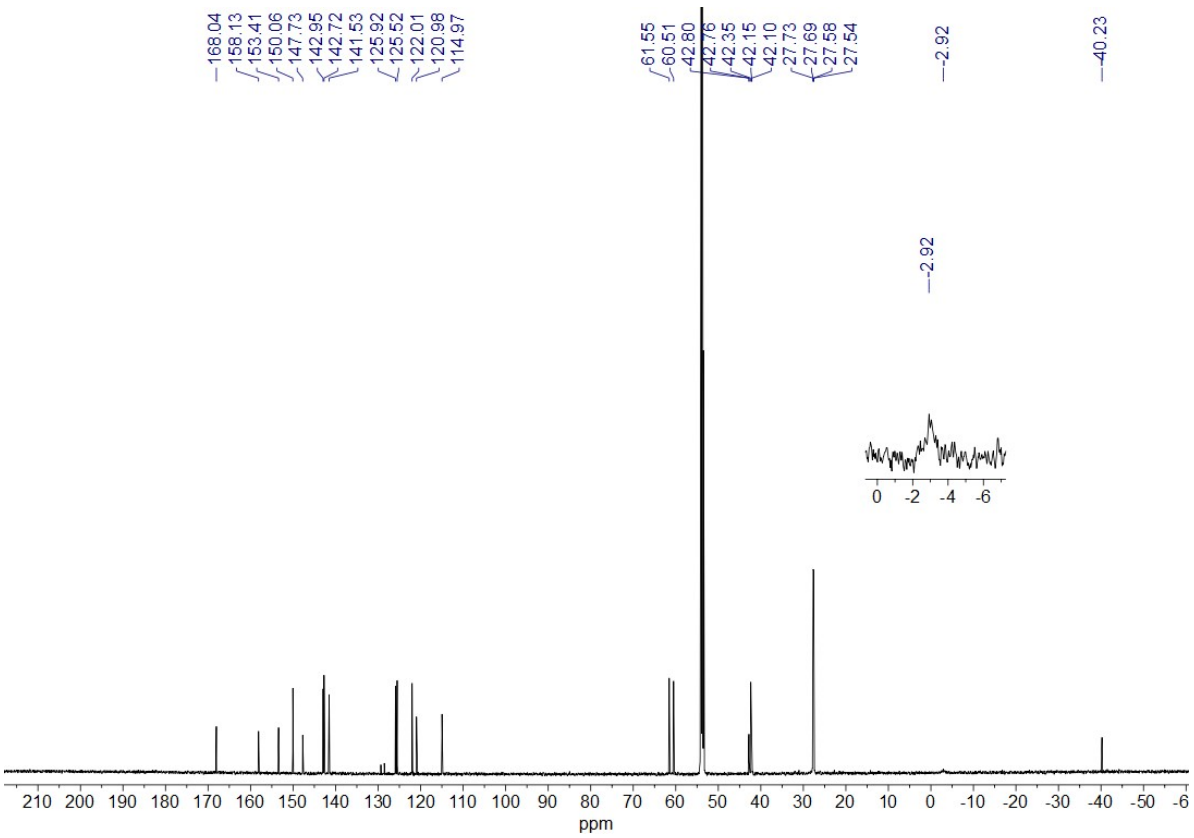

Figure S13. $^{13}C\{^{1}H\}$ NMR spectrum of **3** in CD_2Cl_2 at 25 °C.

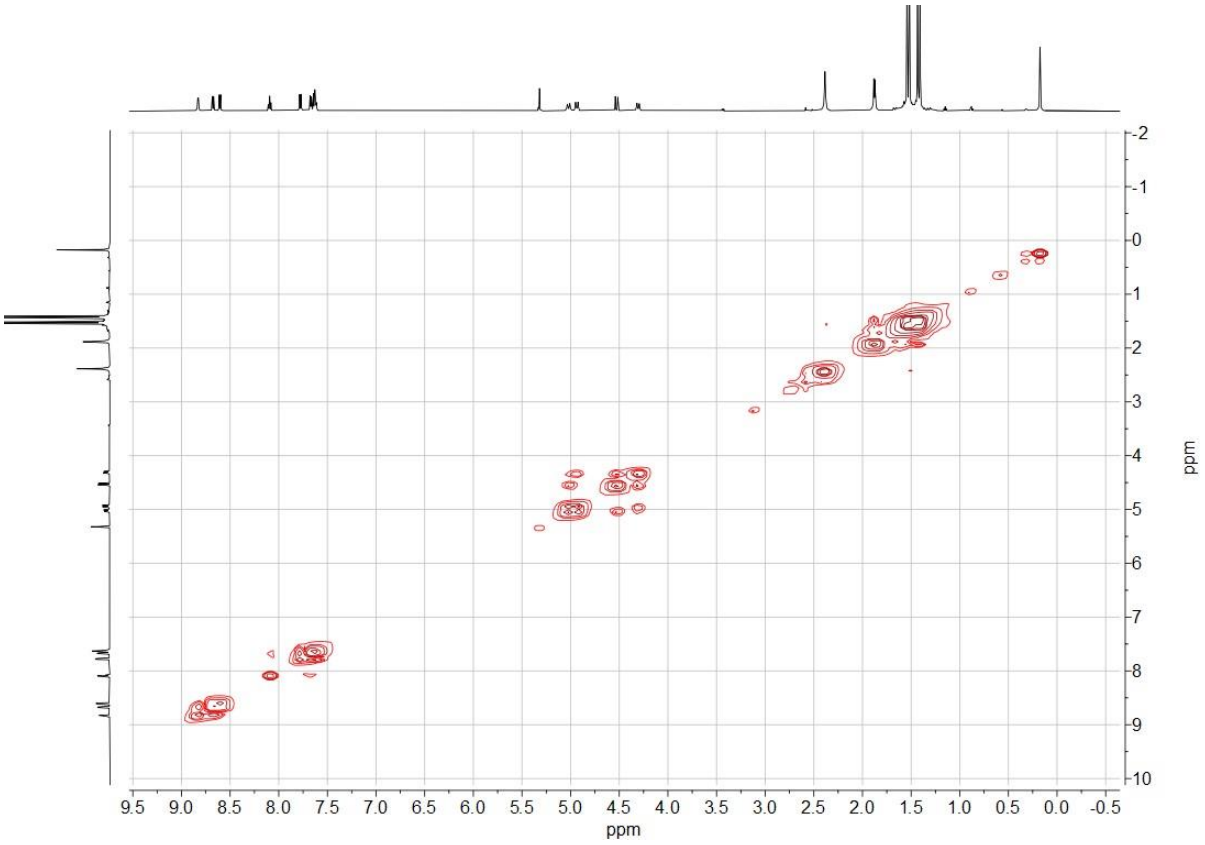

Figure S14. ^{1}H-^{1}H COSY spectrum of **3** in CD_2Cl_2 at 20 °C.

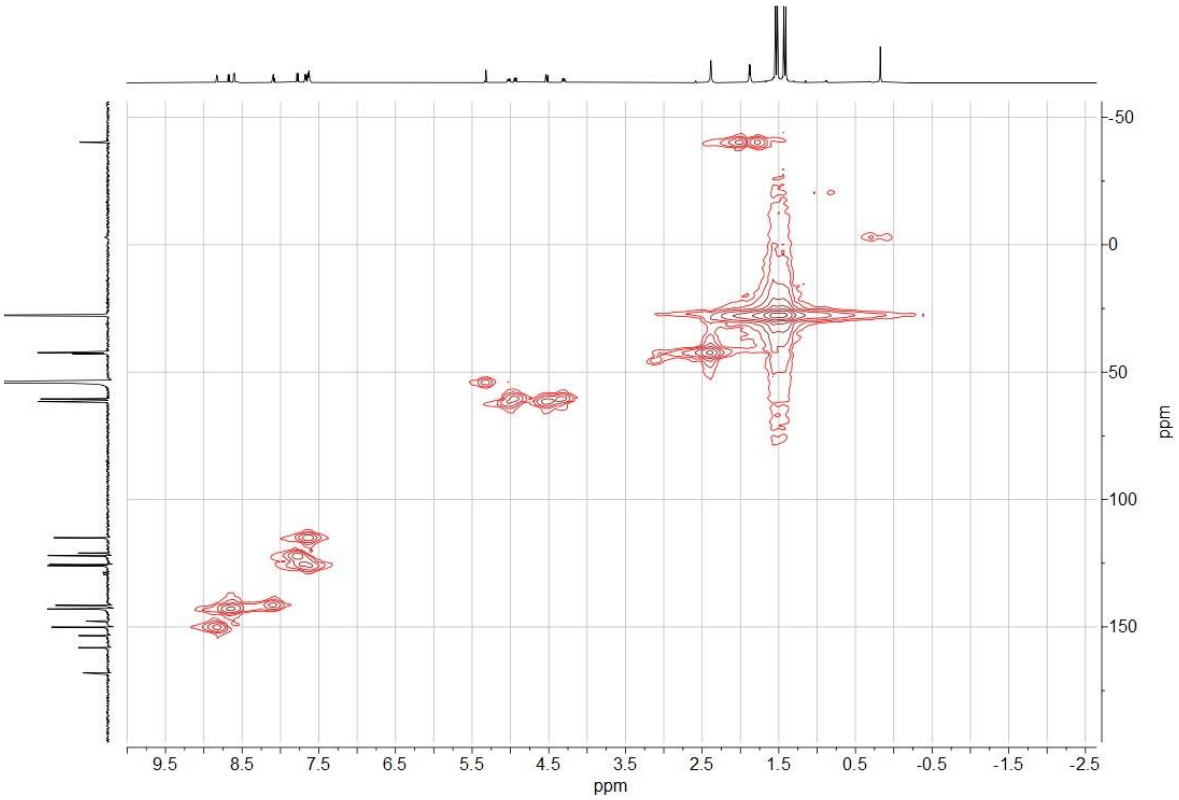

Figure S15. ^{1}H-^{13}C HMQC spectrum of **3** in CD_2Cl_2 at 20 °C.

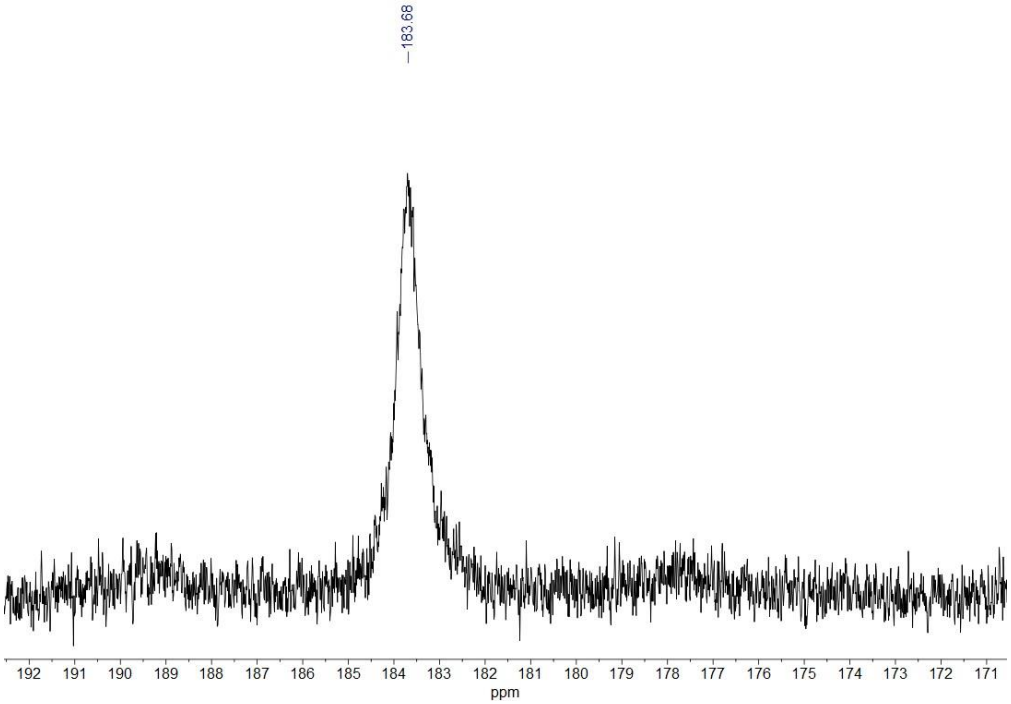

Figure S16. $^{31}P\{^{1}H\}$ NMR spectrum of **3** in CD_2Cl_2 at 20 °C.

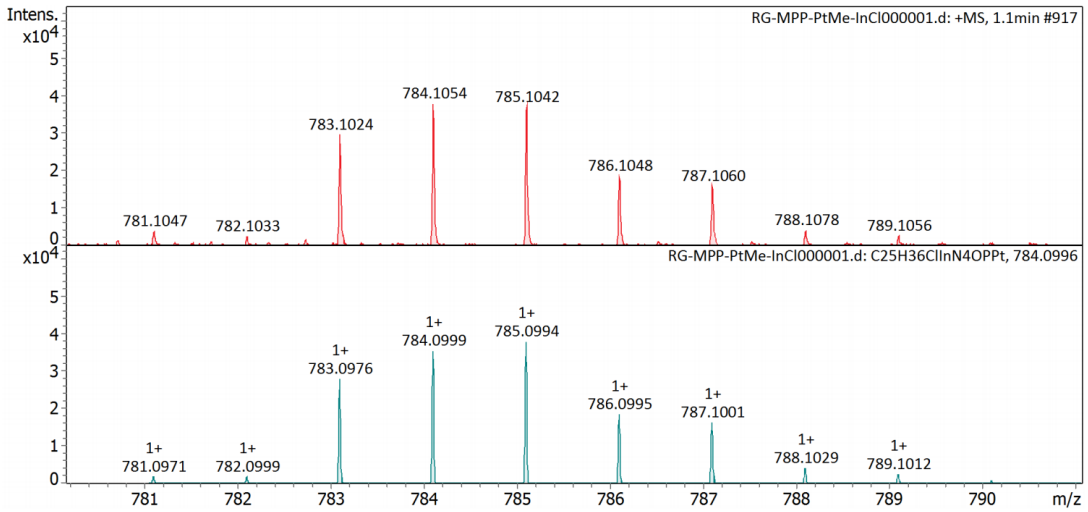

Figure S17. Positive mode ESI-(HR)MS spectrum of a acetonitrile solution of **3** (top) and simulated spectrum for $[(L)PtMeInCl]^{+}[CH_3InCl_3]^{-}$, $C_{25}H_{36}O_1N_4P^{195}PtCl^{115}In^{+}$ (bottom).

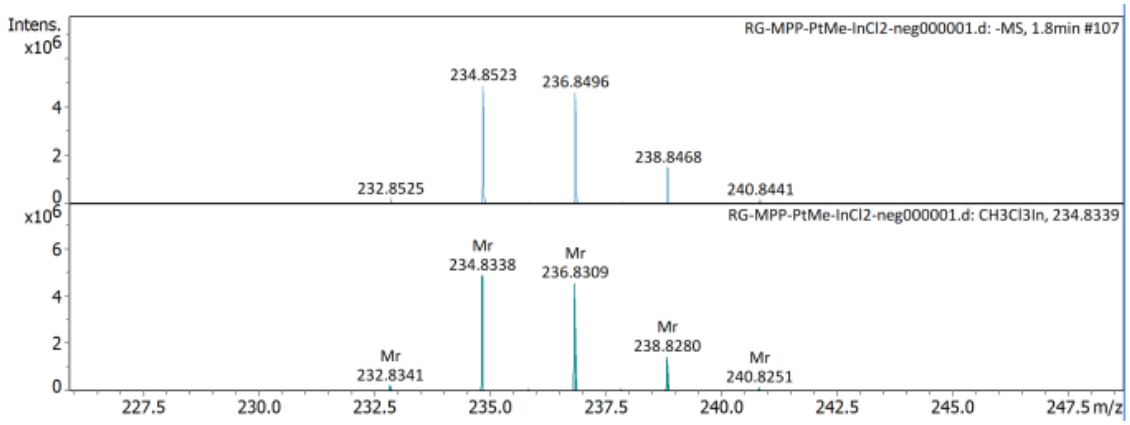

Figure S18. Negative mode ESI-(HR)MS spectrum of a acetonitrile solution of **3** (top) and simulated spectrum for $[(L)PtMeInCl]^{+}[CH_3InCl_3]^{-}$, $CH_3Cl_3{}^{115}In^{-}$ (bottom).

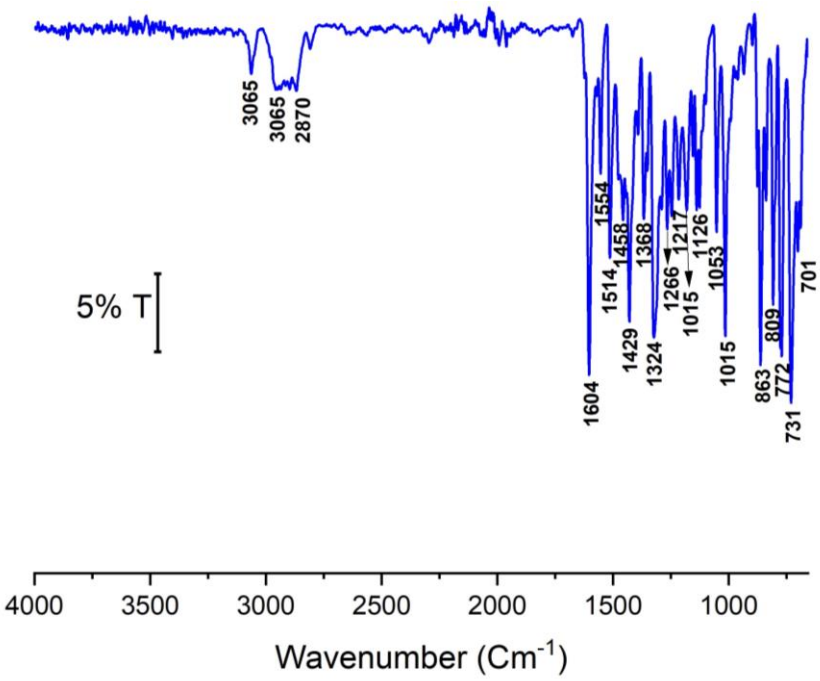

Figure S19. ATR FT-IR transmittance spectrum of **3**.

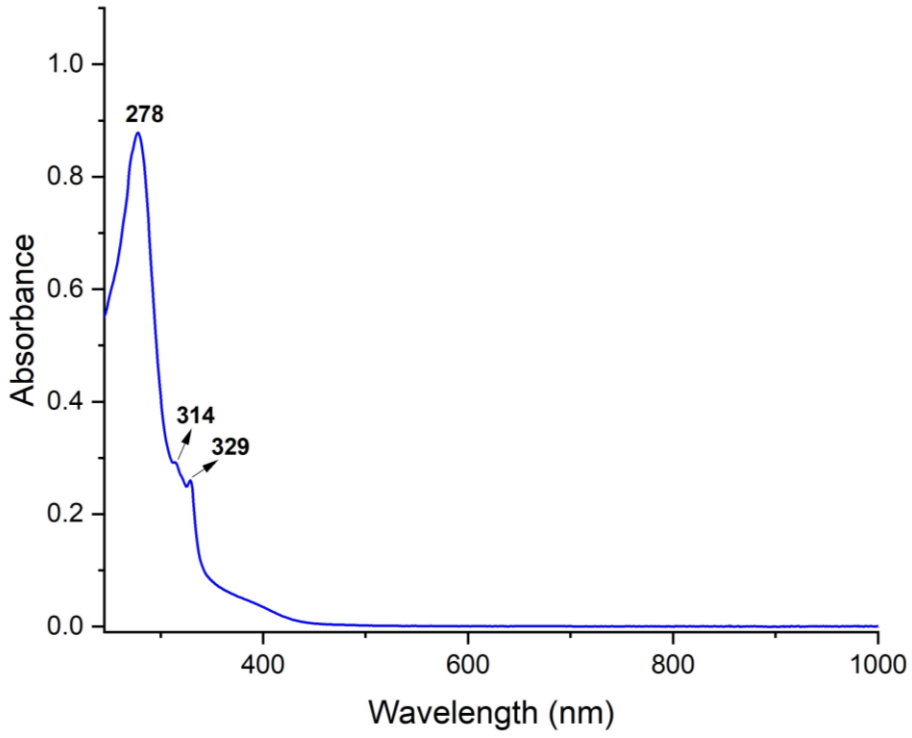

Figure S20. UV-vis absorbance spectrum for **3** (23.5×10^{-6} M) in dichloromethane.

NMR monitoring of the formation of 3 in situ

To a solution of **1** (6.5 mg, 0.01 mmol) in CD_2Cl_2 (0.5 mL) in a J. Young NMR tube, $InCl_2$ (4 mg, 0.022 mmol) was added, and the reaction was monitored with ^1H NMR spectrum, which showed the clean formation of $InCH_3$ as a characteristic peak at 0.18 ppm after 5 min.

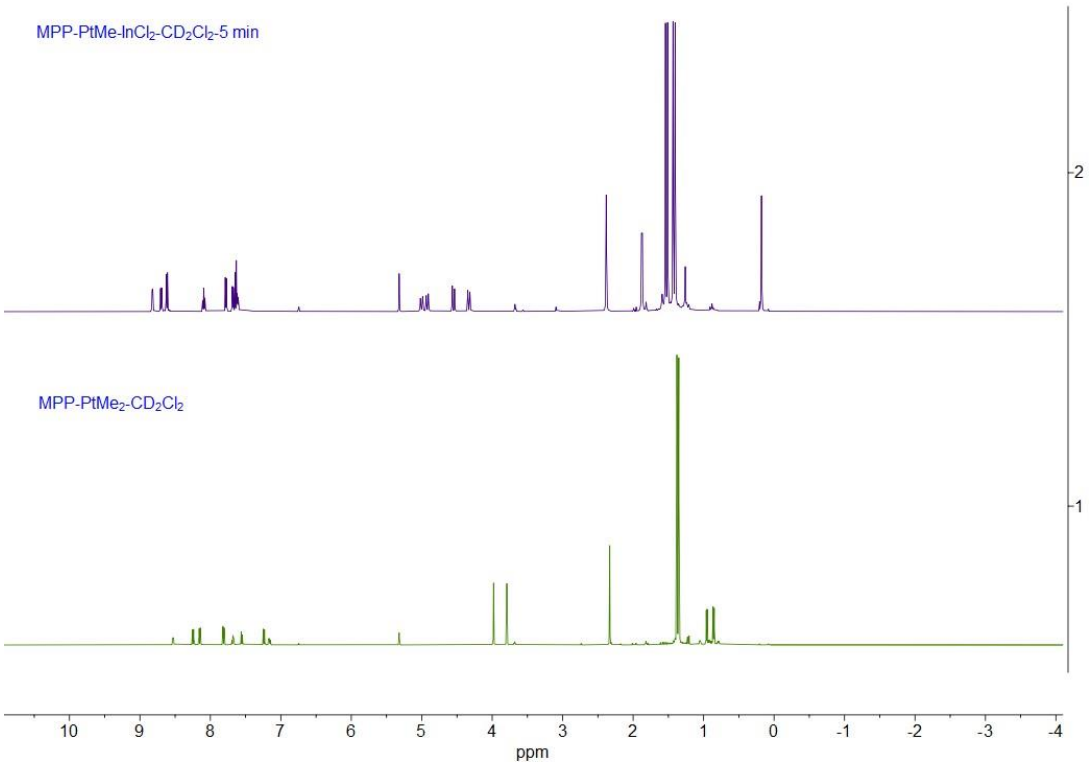

Figure S21. Full ^1H NMR spectrum of **1** (bottom) and **1** after reaction with $InCl_2$ for 5 min (top) in CD_2Cl_2 at 25 °C.

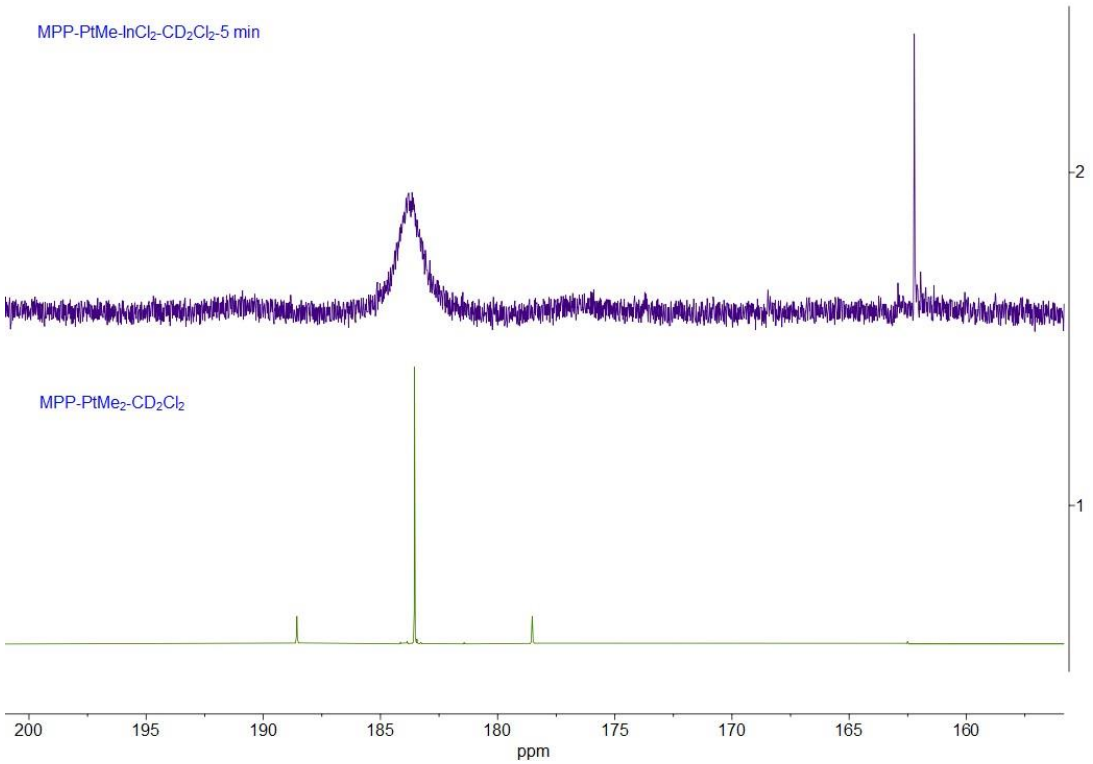

Figure S22. Full ^{31}P NMR spectrum of **1** (bottom) and **1** after reaction with $InCl_2$ for 5 min (top) in CD_2Cl_2 at 25 °C.

Synthesis of [(L)InCl$_2$(μ-Cl)PtMe][InMeCl$_3$], 4

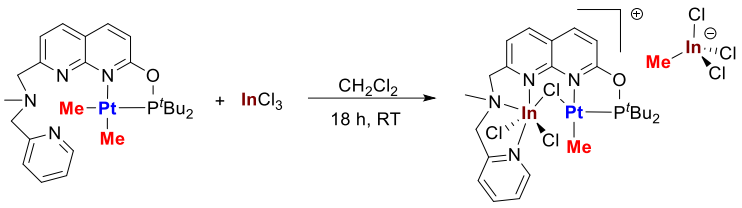

Scheme S3. Formation of **4**.

In Ar filled glovebox, complex **1** (65 mg, 0.1 mmol), $InCl_3$ (45 mg, 0.2 mmol) were placed in a 20 mL vial. To the solid mixture 3 mL of dichloromethane was added and the mixture was left stirring for 18 h at room temperature (RT). The solvent was evaporated under vacuum and the remaining yellow solid was washed with 5 mL of diethyl ether, obtaining pure complex **4**, in 95% yield (108 mg). The crystals of complex **4** were obtained by dissolving **4** in acetonitrile and diffusing the solution with diethyl ether.

^{1}H NMR (500 MHz, CD_2Cl_2, 25 °C) δ 8.92 (dd, J = 5.5, 1.6 Hz, 1H, CH_{Naph}), 8.65 (t, J = 9.0 Hz, 2H, CH_{Py}), 8.14 (td, J = 7.7, 1.7 Hz, 1H, CH_{Naph}), 7.72 (t, J = 8.5 Hz, 2H, CH_{Naph} & CH_{Py}), 7.66 (d, J = 8.7 Hz, 1H, CH_{Py}), 7.64 – 7.59 (m, 1H, CH_{Naph}), 5.09 (d, J = 17.4 Hz, 1H, CH_2), 4.81 – 4.67 (m, 2H, CH_2), 4.60 (d, J = 14.8 Hz, 1H, CH_2), 2.92 (s, 3H, N-CH_3), 1.63 (d, J = 16.3 Hz, 9H), 1.43 (d, J = 16.3 Hz, 9H), 1.13 (d, $^3J_{PH}$= 1.7 Hz, $^2J_{PtH}$ = 66.4 Hz, 3H, Pt-Me), 0.32 (s, 3H, In-Me).

^{13}C{^{1}H} NMR (126 MHz, CD_2Cl_2, 25 °C) δ 166.78 (Cq, $_{Naph}$), 159.69 (Cq, $_{Naph}$), 153.99 (Cq, $_{Py}$), 151.09 (Cq, $_{Naph}$), 147.98 (C_H, $_{Naph}$), 144.51(C_H, $_{Py}$), 144.00 (C_H, $_{Py}$), 142.79 (C_H, $_{Naph}$), 126.51(C_H, $_{Naph}$), 126.06 (C_H, $_{Py}$), 123.26 (C_H, $_{Naph}$), 123.04 (C_H, $_{Py}$), 115.66 (C_H, $_{Naph}$), 62.53 (CH_2), 61.22 (CH_2), 47.06 (N-CH_3), 42.17 (dd, J = 31.0, 26.6 Hz, (***C***$(CH_3)_3$), 27.98 (dd, J = 19.2, 3.7 Hz, C(***C***$H_3)_3$), -1.75 (In-CH_3), -20.92 (d, $^1J_{PtC}$ = 639.4 Hz, $^2J_{PC}$ = 6.5 Hz, Pt-Me).

^{31}P{^{1}H} NMR (243 MHz, CD_2Cl_2, 25 °C) δ: 159.8 ($^1J_{PtP}$ = 5298 Hz).

^{195}Pt{^{1}H} NMR (129 MHz, CD_2Cl_2, 25 °C) δ -4176.79 (d, $^1J_{PtP}$ = 5296 Hz).

ESI-HRMS (m/z pos): Found (Calcd): $[(L)PtMeInCl_3]^+[CH_3InCl_3]^-$,

$C_{25}H_{36}O_1N_4P^{195}PtCl_3{}^{115}In^+$: 854.0316 (854.0375).

ESI-HRMS (m/z neg): Found (Calcd): $[(L)PtMeInCl_3]^+[CH_3InCl_3]^-$, $CH_3Cl_3{}^{115}In^-$: 234.8411 (234.8343).

FT-IR (ATR, solid): 3076 (br, w), 2965(br, w), 2900 (br, w), 1608 (s), 1550 (m), 1517 (s), 1434 (br, m), 1347 (s), 1314 (br, m), 1250 (w), 1185 (w), 1148 (w), 1049 (w), 1023 (m), 871 (s), 805 (s), 779 (s), 732 (m) cm^{-1}.

UV-vis (CH_2Cl_2), λ, nm (ε, $M^{-1}\cdot cm^{-1}$) : 254 (12261), 324 (10405).

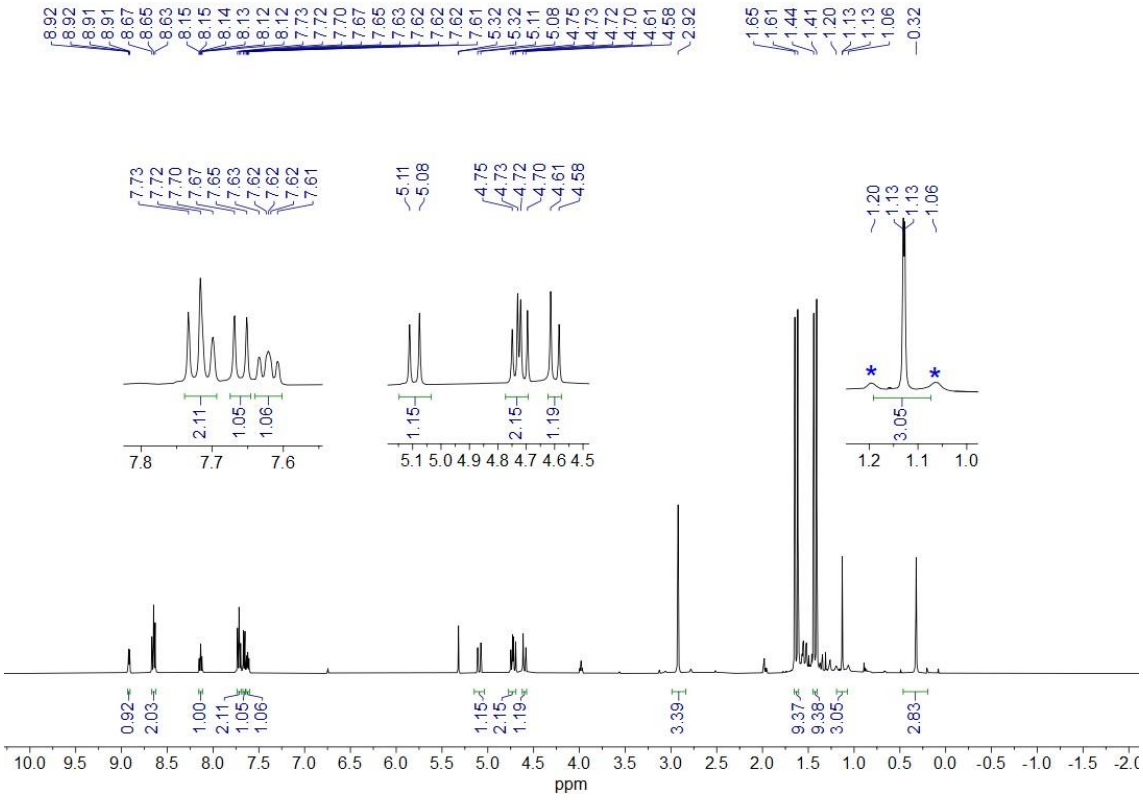

Figure S23. ^1H NMR spectrum of **4** in CD_2Cl_2 at 25 °C. Pt satellites are marked with stars.

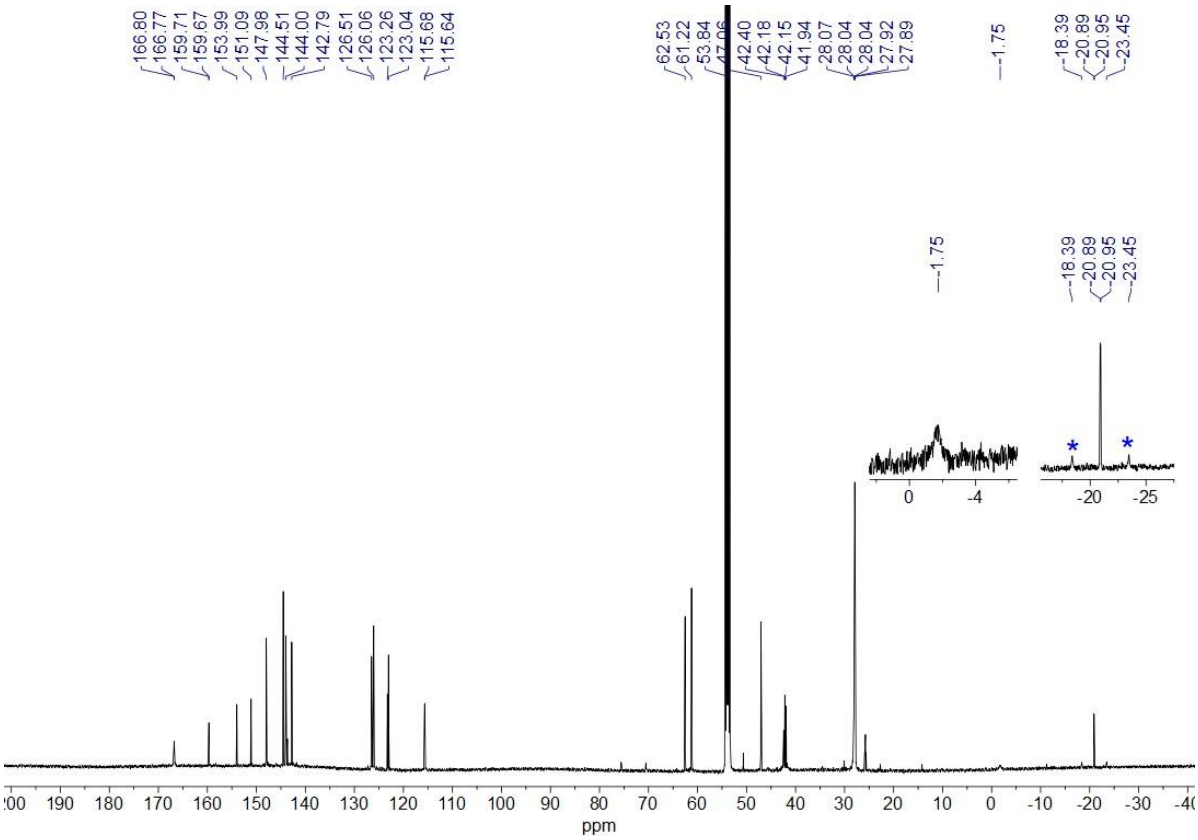

Figure S24. $^{13}C\{^{1}H\}$ NMR spectrum of **4** in CD_2Cl_2 at 25 °C. Pt satellites is marked with stars.

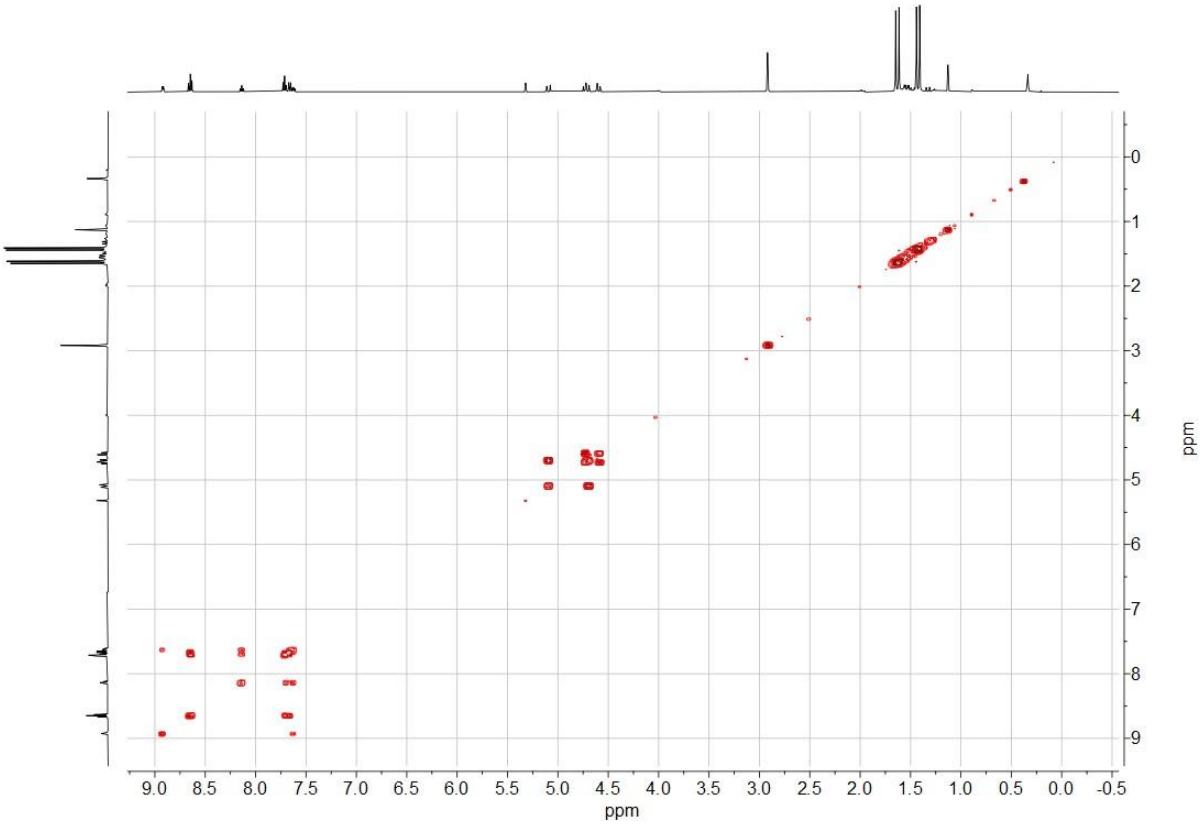

Figure S25. ^{1}H-^{1}H COSY spectrum of **4** in CD_2Cl_2 at 25 °C.

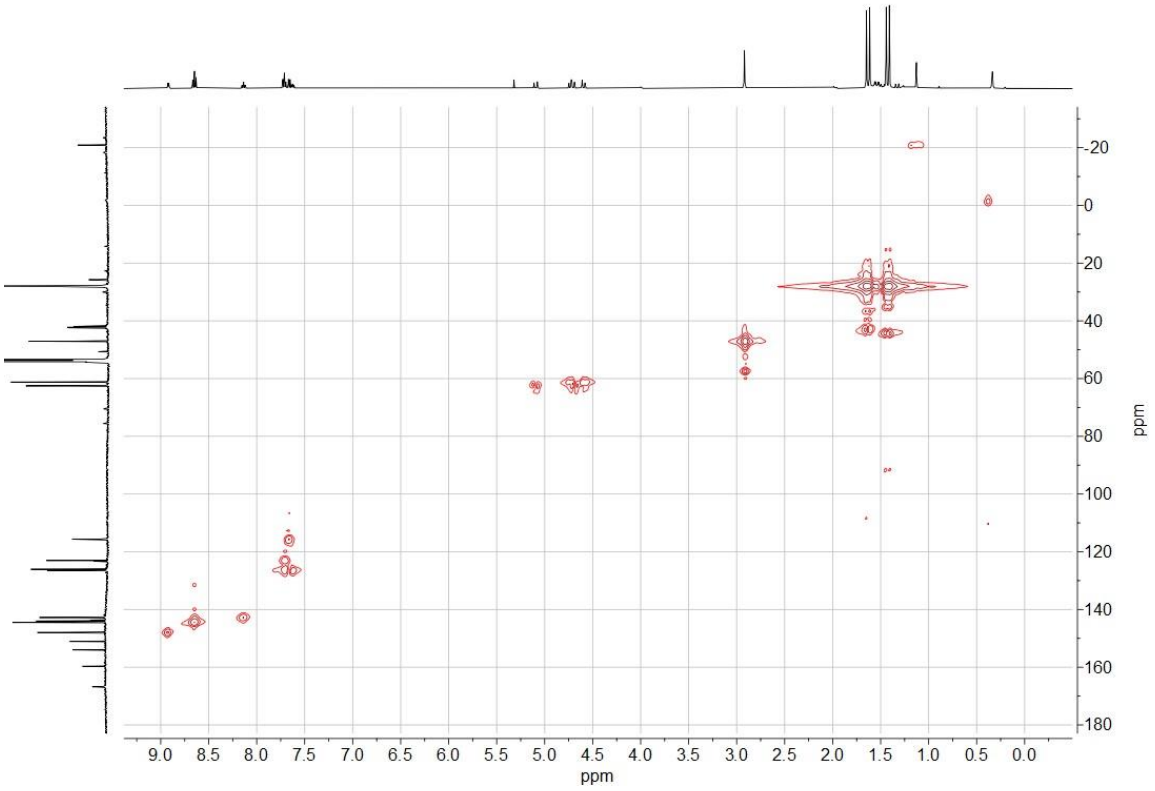

Figure S26. ^{1}H-^{13}C HMQC spectrum of **4** in CD_2Cl_2 at 25 °C.

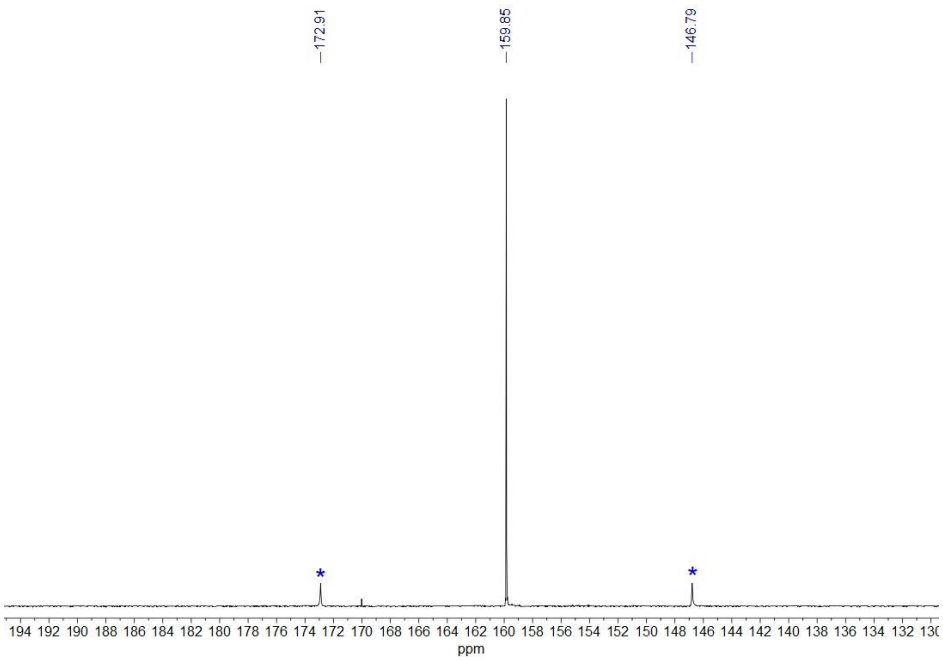

Figure S27. $^{31}P\{^{1}H\}$ NMR spectrum of **4** in CD_2Cl_2 at 25 °C. Pt satellites are marked with stars.

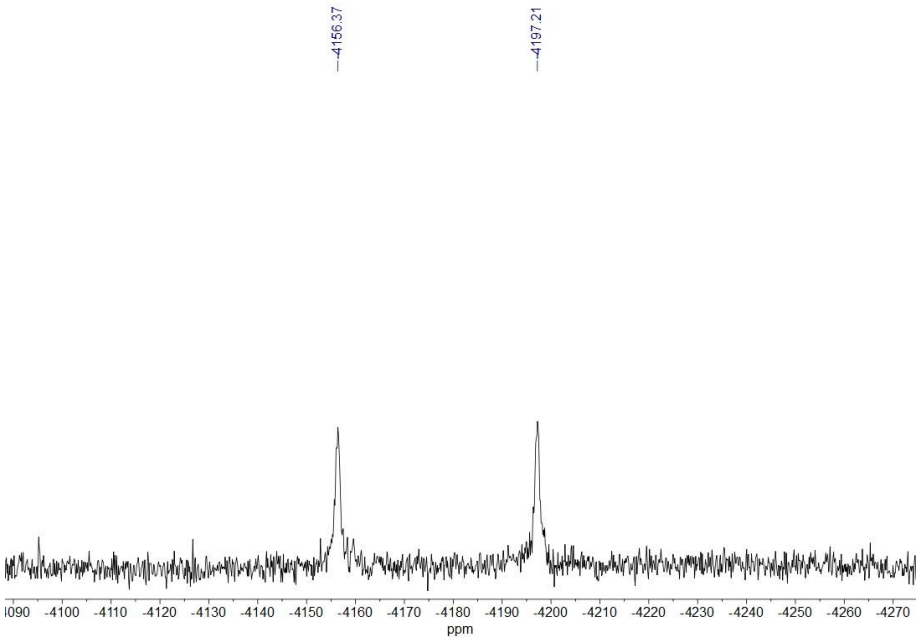

Figure S28. $^{195}Pt\{^{1}H\}$ NMR spectrum of **4** in CD_2Cl_2 at 25 °C.

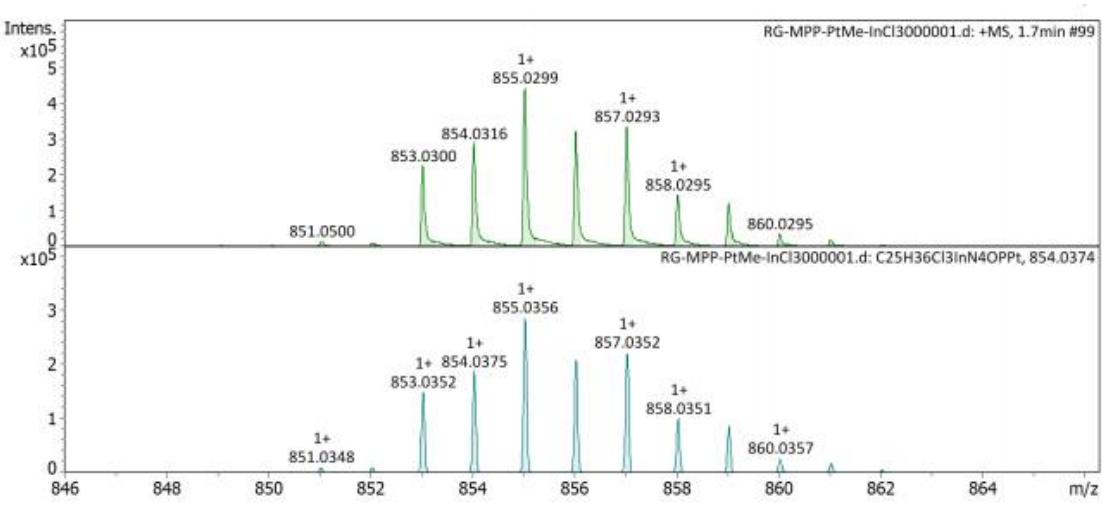

Figure S29. ESI-(HR)MS spectrum of a acetonitrile solution of **4** (top) and simulated spectrum for $[(L)PtMeInCl_3]^+[CH_3InCl_3]^-$, $C_{25}H_{36}O_1N_4P^{195}PtCl_3{}^{115}In^+$ (bottom).

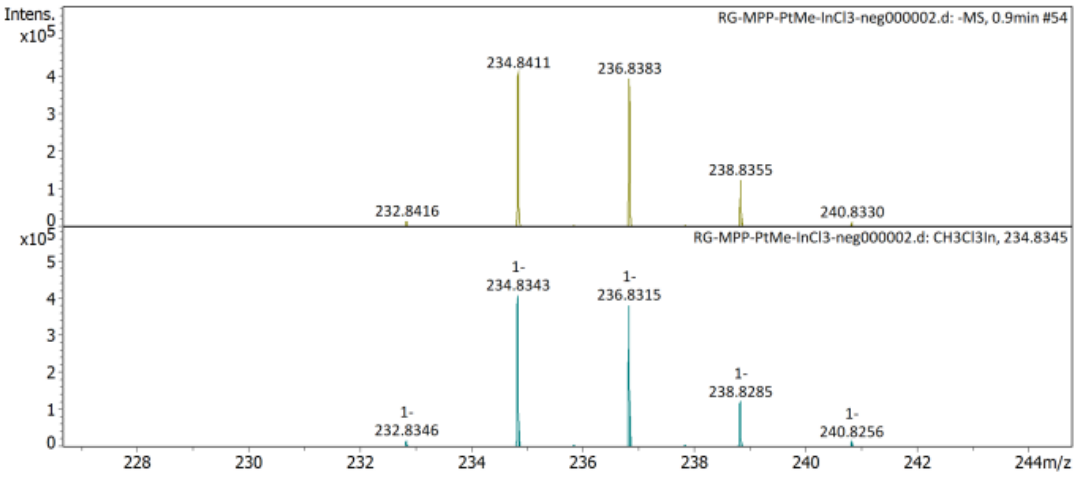

Figure S30. ESI-(HR)MS spectrum of a acetonitrile solution of **4** (top) and simulated spectrum for $[(L)PtMeInCl_3]^+[CH_3InCl_3]^-$, $CH_3Cl_3{}^{115}In^-$ (bottom).

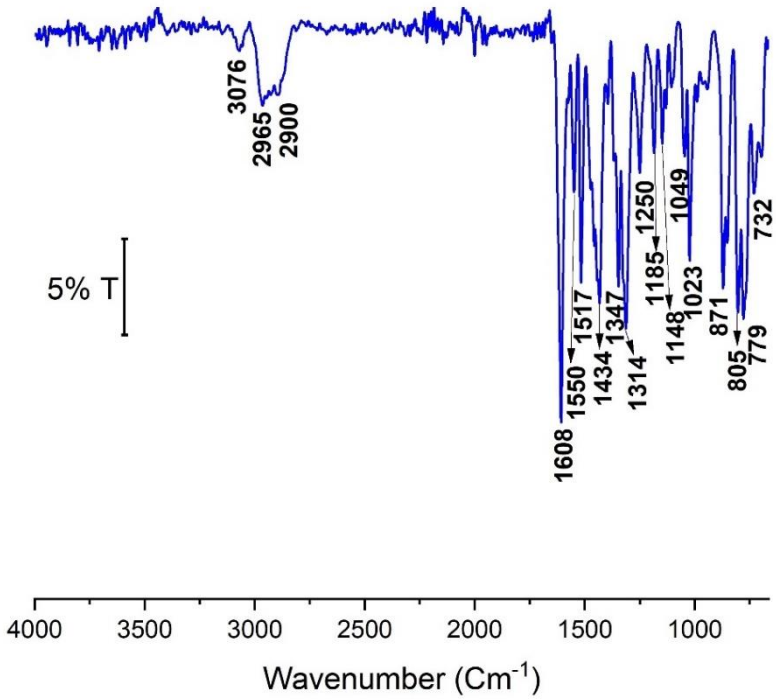

Figure S31. ATR FT-IR transmittance spectrum of **4**.

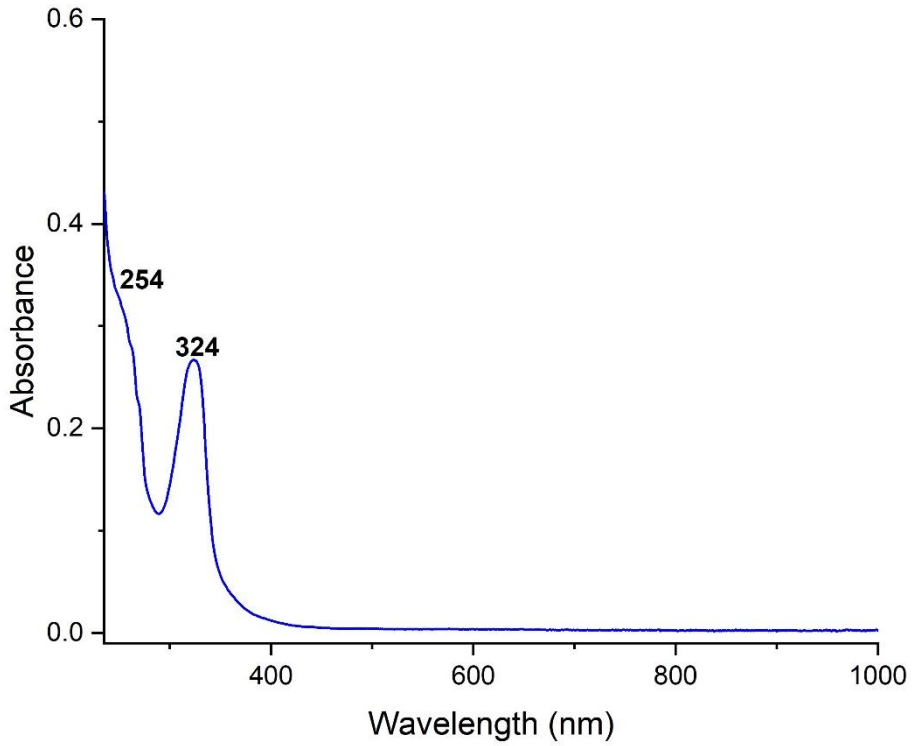

Figure S32. UV-vis absorbance spectrum for **4** (25.6 x 10^{-6} M) in dichloromethane.

NMR monitoring of the formation of 4 in situ

To a solution of **1** (6.5 mg, 0.01 mmol) in CD_2Cl_2 (0.5 mL) in a J. Young NMR tube, $InCl_3$ (5 mg, 0.022 mmol) was added, and the reaction was monitored with ^1H NMR spectrum, which showed the clean formation of $InCH_3$ as a characteristic peak at 0.34 ppm.

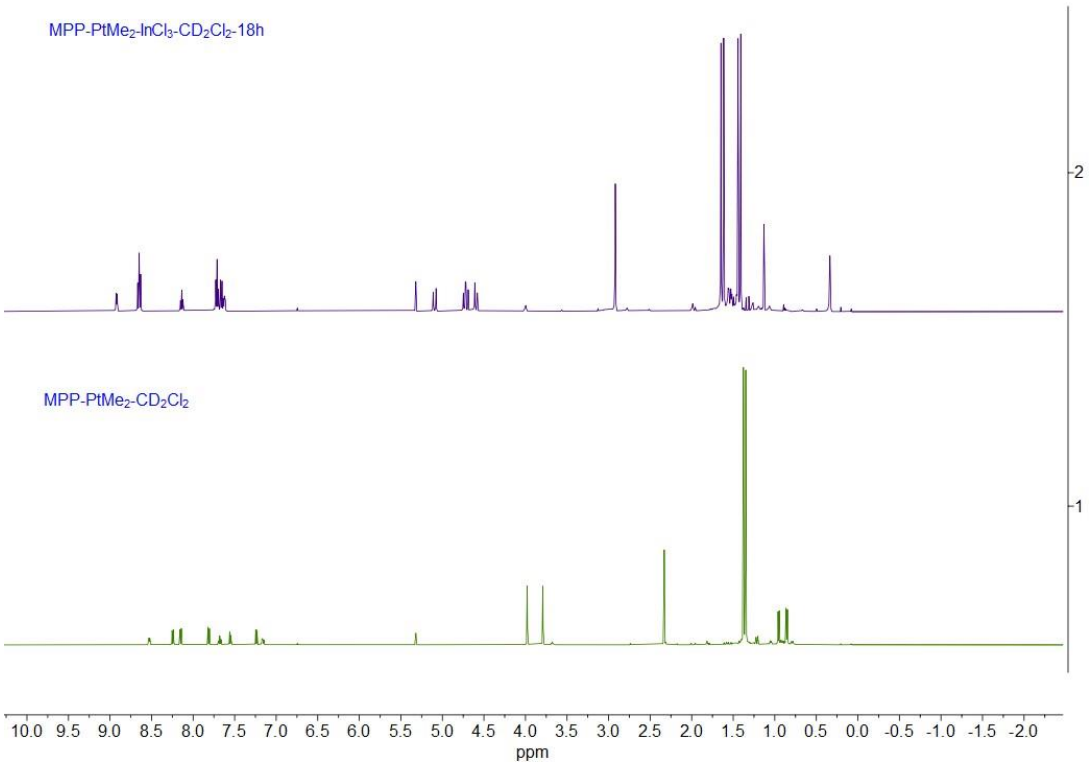

Figure S33. Full ^1H NMR spectrum of **1** (bottom) and $InCl_3$ after reaction with $InCl_3$ for 18 h (top) in CD_2Cl_2 at 25 °C.

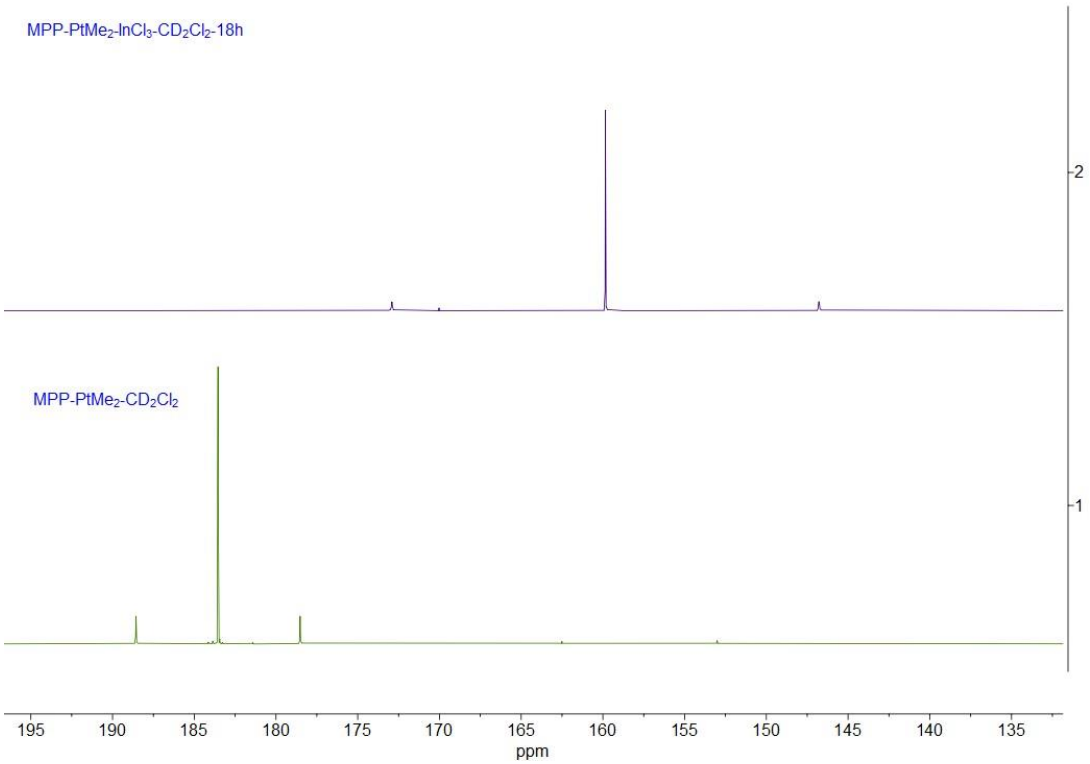

Figure S34. Full $^{31}P\{^{1}H\}$ NMR spectrum of **1** (bottom) and **1** after reaction with $InCl_3$ for 18 h (top) in CD_2Cl_2 at 25 °C.

Computational details

All calculations were performed using density functional theory (DFT) using the Gaussian 16 package.[2] Geometry optimizations and frequency analyses for cationic parts of all complexes used in QTAIM and NBO analyses were carried out in the gas-phase without symmetry restrictions using the ωB97XD functional[3] and def2-tzvp basis set[4] for all elements as implemented in Gaussian 16. Ground states corresponded to the absence of imaginary frequencies. The initial atomic coordinates were taken from the crystal structures determined by SC-XRD. All geometries are provided as XYZ files.

The quantum-topological analysis of the calculated electron density of the "gas-phase" structures was performed within the quantum topological theory of atoms in molecules by means of the *AIMAll* package (v 19.10.12).[5]

According to Quantum Theory of Atoms in Molecules (QTAIM),[6] the bonding between two atoms is indicated by the presence of a bond critical point, *bcp* (in other words, a (3,-1) critical point of $\rho(\boldsymbol{r})$) along a bond path connecting two neighbouring atoms. The character of the bonding can be characterized by local indicators at the bcp and by the electron delocalization indices (DIs, an average number of electrons shared between pair of atoms) related to the degree of covalence and bond multiplicity.[7] Negative and positive values of the Laplacian at the bcp, $\nabla^2\rho_b$, are characteristics of "shared" and "closed-shell" interactions, respectively.[7-8] The value of ρ at bcp, ρ_b, is characteristic of a bond strength.[9] Metal-metal and metal-ligand interactions are typically characterized by positive values of $\nabla^2\rho_b$ and low ρ_b.[7, 10] Other characteristics are H_b (total energy density, $G_b + V_b$), G_b (kinetic energy density), V_b (potential energy density) at bcp and the relative ratio of the latter two, $|V_b|/G_b$. The covalent bonds are characterized by $|V_b|/G_b > 2$, the intermediate or transit region is characterized by $1 < |V_b|/G_b < 2$.[11]

Multiwfn was used to build real-space function maps.[12]

NBO analysis was performed using NBO 7.0[13] The NBO orbitals were visualized using ChemCraft.[14]

Table S1. Selected bond critical point (*bcp*) properties for Pt−E (E = Ga or In) bonds in geometry-optimized[a] cationic parts of complexes **2** and **3**.

Complex	ρ_b [b]	$\nabla^2\rho_b$ [c]	H_b [d]	$\lvert V_b\rvert/G_b$ [e]	DI [f]
2	0.082276	0.009362	-0.034248	1.94	0.877468
3	0.071005	0.057715	-0.02342	1.62	0.861053

[a] At ωB97XD/def2-tzvp level. [b] Electron density (a.u.). [c] Laplacian of electron density (a.u.). [d] The total energy density density (a.u.). [e] Ratio between the absolute electronic potential energy and kinetic energy densities. [f] Delocalization index.

QTAIM analysis

Complex **2**:

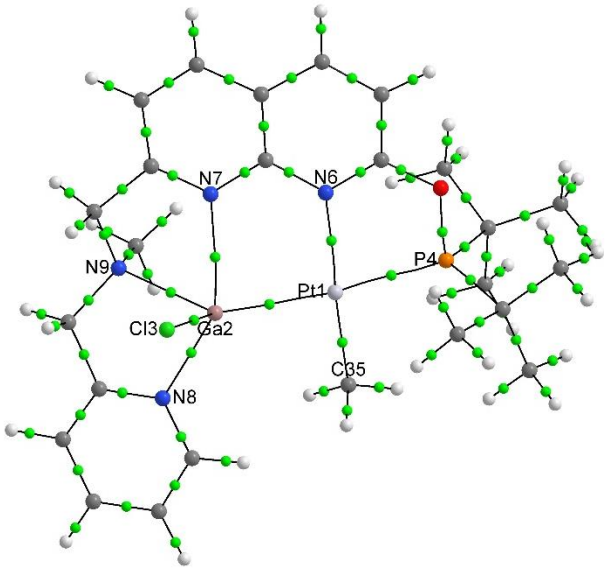

Figure S35. Molecular graph for "gas-phase" DFT-optimized cationic part of complex **2**. Bond critical points (3, –1) with a threshold of electron density above 0.025 a.u. and corresponding bond paths are shown with green dots and black lines, respectively.

Table S2. Quantum-topological parameters [in a.u.] at the bond critical points involving metal atoms for "gas-phase" DFT-optimized **2**.

Bonding atoms	ρ_b[a]	$\nabla^2\rho_b$[b]	ε[c]	λ_1[d]	λ_2[d]	λ_3[d]	V_b[e]	G_b[f]	H_b[g]	DI[h]
Pt1 - P4	0.114761	0.117341	0.016255	-0.098072	-0.096503	0.311916	-0.13789	0.083568	-0.054322	0.950017
Pt1 - N6	0.085231	0.338509	0.009814	-0.073944	-0.073226	0.485679	-0.12596	0.105208	-0.020754	0.60397
Pt1 - Ga2	0.082276	0.009362	0.033426	-0.063987	-0.061917	0.135265	-0.07083	0.036585	-0.034248	0.877468
Pt1 - C35	0.138997	0.054085	0.001591	-0.166904	-0.166639	0.387629	-0.15497	0.08415	-0.070818	1.027566
Ga2 - N9	0.052138	0.127503	0.007086	-0.056196	-0.055801	0.2395	-0.0539	0.042886	-0.01101	0.25826
Ga2 - N8	0.062383	0.185741	0.047708	-0.073402	-0.07006	0.329202	-0.07106	0.058746	-0.012311	0.325052
Ga2 - N7	0.0415	0.098344	0.132438	-0.039868	-0.035206	0.173418	-0.0388	0.031692	-0.007106	0.211914
Ga2 - Cl3	0.081394	0.208964	0.019478	-0.086275	-0.084627	0.379865	-0.10065	0.076446	-0.024205	0.580085

[a]Electron density; [b]Laplacian of electron density; [c]Bond ellipticity; [d]Eigenvalues of the Hessian matrix of $\rho(\boldsymbol{r})$ at the bcp; [e]Potential energy density; [f]Kinetic energy density; [g]Total energy density; [h]Delocalization index. All values are given for the corresponding bcps.

Complex 3

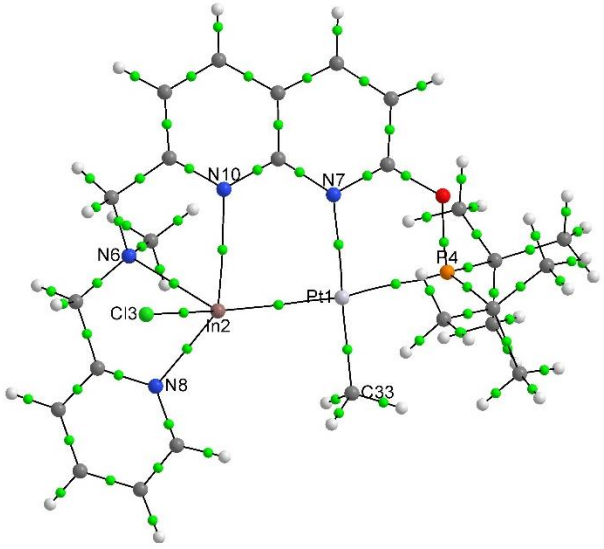

Figure S36. Molecular graph for "gas-phase" DFT-optimized cationic part of complex **3**. Bond critical points (3, –1) with a threshold of electron density above 0.025 a.u. and corresponding bond paths are shown with green dots and black lines, respectively.

Table S3. Quantum-topological parameters [in a.u.] at the bond critical points involving metal atoms for "gas-phase" DFT-optimized **3**.

Bonding atoms	ρ_b[a]	$\nabla^2\rho_b$[b]	ε[c]	λ_1[d]	λ_2[d]	λ_3[d]	V_b[e]	G_b[f]	H_b[g]	DI[h]
Pt1 - P4	0.122221	0.101066	0.011644	-0.106093	-0.104872	0.31203	-0.14863	0.086897	-0.06173	0.997201
Pt1 - N7	0.080364	0.316387	0.017087	-0.067735	-0.066597	0.450718	-0.11576	0.097357	-0.0184	0.584651
Pt1 - In2	0.071005	0.057715	0.030327	-0.051717	-0.050195	0.159626	-0.06127	0.037847	-0.02342	0.861053
Pt1 - C33	0.138951	0.043817	0.005478	-0.168468	-0.167551	0.379836	-0.15255	0.081663	-0.07089	1.027815
In2 - N8	0.053018	0.162754	0.037703	-0.058021	-0.055913	0.276687	-0.05639	0.04854	-0.00785	0.321015
In2 - N6	0.042653	0.118346	0.003387	-0.043247	-0.043101	0.204695	-0.04049	0.03504	-0.00545	0.237868
In2 - N10	0.037857	0.112959	0.046797	-0.035756	-0.034157	0.182873	-0.03453	0.031383	-0.00314	0.224961
In2 - Cl3	0.072335	0.186004	0.004909	-0.070285	-0.069942	0.32623	-0.08449	0.065497	-0.019	0.622355

[a]Electron density; [b]Laplacian of electron density; [c]Bond ellipticity; [d]Eigenvalues of the Hessian matrix of $\rho(\boldsymbol{r})$ at the bcp; [e]Potential energy density; [f]Kinetic energy density; [g]Total energy density; [h]Delocalization index. All values are given for the corresponding bcps.

Complex 4

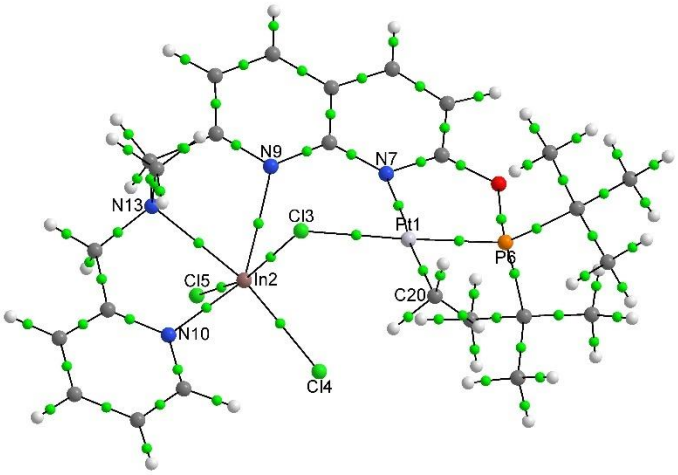

Figure S37. Molecular graph for "gas-phase" DFT-optimized cationic part of complex **4**. Bond critical points (3, –1) with a threshold of electron density above 0.025 a.u. and corresponding bond paths are shown with green dots and black lines, respectively.

Table S4. Quantum-topological parameters [in a.u.] at the bond critical points involving metal atoms for "gas-phase" DFT-optimized **4**.

Bonding atoms	ρ_b[a]	$\nabla^2\rho_b$[b]	ε[c]	λ_1[d]	λ_2[d]	λ_3[d]	V_b[e]	G_b[f]	H_b[g]	DI[h]
Pt1-P6	0.145948	0.014049	0.010126	-0.13372	-0.13238	0.280141	-0.18225	0.092815	-0.08944	1.139849
Pt1-N7	0.065323	0.253858	0.01873	-0.05184	-0.05089	0.356591	-0.08682	0.07511	-0.01171	0.492833
Pt1-Cl4	0.012959	0.03793	0.271529	-0.0073	-0.00574	0.05097	-0.00811	0.008797	0.000685	0.124914
Pt1-Cl3	0.07235	0.204718	0.139063	-0.06453	-0.05665	0.325894	-0.08936	0.070235	-0.01912	0.640307
Pt1-C20	0.144301	0.010546	0.019228	-0.18307	-0.17962	0.37324	-0.15642	0.079448	-0.07697	1.023156
In2-N9	0.040823	0.118722	0.039248	-0.04175	-0.04017	0.200636	-0.03824	0.033958	-0.00428	0.231948
In2-N13	0.049802	0.132765	0.012233	-0.05335	-0.0527	0.238816	-0.04946	0.041326	-0.00813	0.262119
In2-N10	0.064087	0.200371	0.043506	-0.07567	-0.07251	0.348546	-0.07409	0.062092	-0.012	0.348166
In2-Cl5	0.073884	0.181917	0.010474	-0.07253	-0.07178	0.326226	-0.08581	0.065645	-0.02017	0.587064
In2-Cl4	0.075851	0.187069	0.02143	-0.07532	-0.07374	0.336127	-0.08911	0.06794	-0.02117	0.613351
In2-Cl3	0.053215	0.136514	0.003137	-0.05061	-0.05045	0.237568	-0.05421	0.044168	-0.01004	0.389663

[a]Electron density; [b]Laplacian of electron density; [c]Bond ellipticity; [d]Eigenvalues of the Hessian matrix of $\rho(\boldsymbol{r})$ at the bcp; [e]Potential energy density; [f]Kinetic energy density; [g]Total energy density; [h]Delocalization index. All values are given for the corresponding bcps.

NBO analysis

Complex **2**:

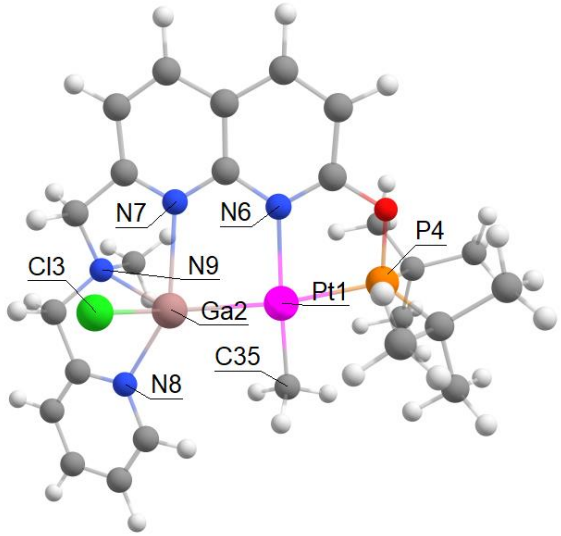

Figure S38. Atom numbering scheme in complex **2** used in NBO analysis.

Selected NLMO (#75) in 3 corresponding to Pt–Ga bonding (individual LMO bond order between Pt and Sn of 0.8689546; other LMO's are characterized by NLMO Pt–Sn bond orders <0.04; net linear NLMO/NPA bond order Pt-Sn 0.7258):[13, 15]

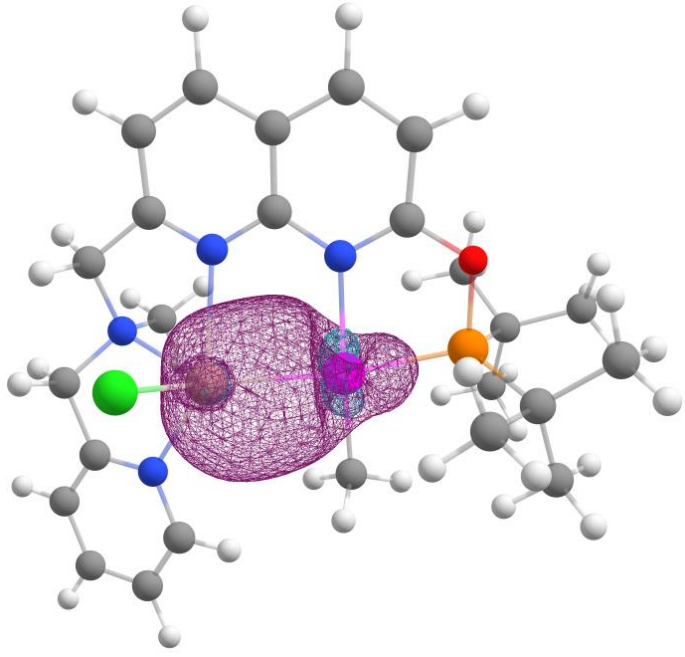

Figure S39. NLMO #75 corresponding to Pt-Ga bonding.

Full composition (contributions >1% are shown in blue):

Hybridization/Polarization Analysis of NLMOs in NAO Basis:

NLMO / Occupancy / Percent from Parent NBO / Atomic Hybrid Contributions

75. (2.00000) 94.7108% BD (1)Pt 1-Ga 2

43.448% Pt 1 s(39.61%)p 0.00(0.20%)d 1.52(60.19%)
f 0.00(0.01%)

53.249% Ga 2 s(77.11%)p 0.29(22.47%)d 0.00(0.38%)
f 0.00(0.04%)

0.059% Cl 3 s(1.29%)p61.62(79.32%)d14.79(19.03%)
f 0.28(0.36%)

0.207% P 4 s(40.80%)p 1.21(49.19%)d 0.24(9.78%)
f 0.01(0.24%)

0.012% O 5 s(46.21%)p 1.08(49.82%)d 0.09(3.94%)
f 0.00(0.03%)

0.385% N 6 s(20.39%)p 3.88(79.10%)d 0.02(0.50%)
f 0.00(0.01%)

0.177% N 7 s(61.33%)p 0.59(35.96%)d 0.04(2.68%)
f 0.00(0.03%)

0.148% N 8 s(35.01%)p 1.80(62.94%)d 0.06(2.01%)
f 0.00(0.04%)

0.075% N 9 s(32.48%)p 2.03(65.93%)d 0.05(1.54%)
f 0.00(0.05%)

0.065% C 10 s(41.16%)p 1.39(57.34%)d 0.03(1.21%)
f 0.01(0.29%)

0.042% C 11 s(28.11%)p 2.47(69.51%)d 0.08(2.17%)
f 0.01(0.21%)

0.104% C 14 s(25.40%)p 2.90(73.60%)d 0.04(0.92%)
f 0.00(0.08%)

0.023% C 17 s(38.30%)p 1.55(59.26%)d 0.06(2.39%)
f 0.00(0.05%)

0.020% C 22 s(20.24%)p 3.84(77.71%)d 0.10(1.99%)
f 0.00(0.06%)

0.100% C 27 s(16.83%)p 4.91(82.58%)d 0.03(0.51%)
f 0.00(0.08%)

0.018% C 28 s(25.42%)p 2.80(71.19%)d 0.11(2.91%)
f 0.02(0.47%)

0.061% C 29 s(6.57%)p13.85(90.98%)d 0.35(2.30%)

		f 0.02(0.15%)
0.019%	C 31 s(26.36%)p 2.50(65.88%)d 0.28(	7.38%)
		f 0.01(0.38%)
1.396%	C 35 s(16.11%)p 5.18(83.42%)d 0.03(	0.47%)
		f 0.00(0.00%)
0.048%	H 36 s(98.87%)p 0.01(	1.13%)
0.145%	H 38 s(99.66%)p 0.00(	0.34%)
0.042%	C 43 s(30.21%)p 2.28(68.99%)d 0.03(	0.76%)
		f 0.00(0.04%)
0.016%	C 44 s(10.04%)p 8.91(89.49%)d 0.03(	0.33%)
		f 0.01(0.14%)
0.024%	C 54 s(42.53%)p 1.29(54.84%)d 0.06(	2.59%)
		f 0.00(0.04%)

Table S5. Natural bond indices (NBI) in complex **2**.

	Pt1	**Ga2**	**C35**	**N6**	**Cl3**	**N7**	**N8**	**N9**
Pt1	-	0.7390	0.8118	0.4672	0.1612	-	-	-
Ga2	0.7390	-	-	-	0.7899	0.3881	0.4591	0.3873

Table S6. Wiberg bond indices (WBI) in complex **2**.

	Pt1	**Ga2**	**C35**	**N6**	**Cl3**	**N7**	**N8**	**N9**
Pt1	-	0.5461	0.6590	0.2183	-	-	-	-
Ga2	0.5461	-	-	-	0.6239	0.1506	0.2108	0.1500

Complex **3**:

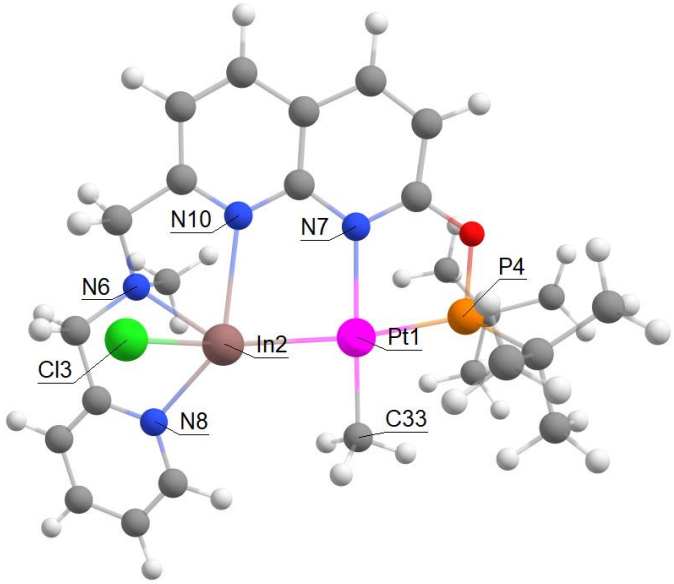

Figure S40. Atom numbering scheme in complex **3** used in NBO analysis.

Selected NLMO (#70) in 3 corresponding to Pt–Sn bonding (individual LMO bond order between Pt and In of 0.8018664; other LMO's are characterized by NLMO Pt–Sn bond orders <0.03; net linear NLMO/NPA order Pt-Sn 0.6500):[13, 15]

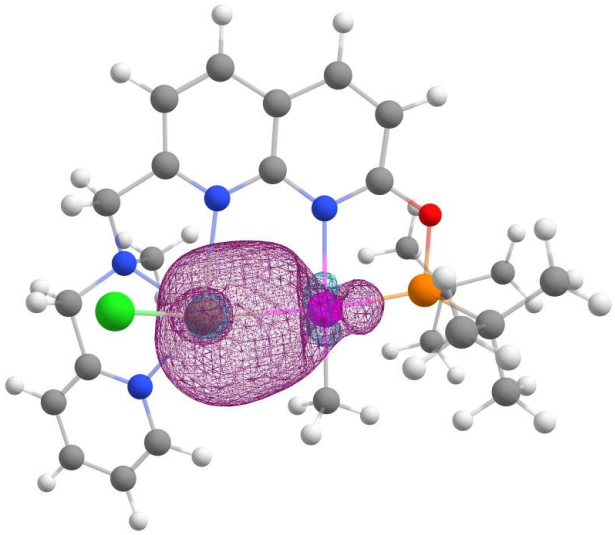

Figure S41. NLMO #70 corresponding to Pt-In bonding**.**

Full composition (contributions >1% are shown in blue):

Hybridization/Polarization Analysis of NLMOs in NAO Basis:

NLMO / Occupancy / Percent from Parent NBO / Atomic Hybrid Contributions

70. (2.00000) 95.4507% BD (1)Pt 1-In 2

40.093% Pt 1 s(41.08%)p 0.00(0.16%)d 1.43(58.75%)
f 0.00(0.01%)

57.030% In 2 s(80.71%)p 0.24(18.98%)d 0.00(0.25%)
f 0.00(0.05%)

0.019% Cl 3 s(2.64%)p21.29(56.26%)d15.41(40.72%)
f 0.14(0.38%)

0.201% P 4 s(47.52%)p 0.90(42.94%)d 0.20(9.34%)
f 0.00(0.20%)

0.010% O 5 s(50.66%)p 0.90(45.58%)d 0.07(3.73%)
f 0.00(0.03%)

0.062% N 6 s(33.44%)p 1.97(65.88%)d 0.02(0.66%)
f 0.00(0.02%)

0.337% N 7 s(19.30%)p 4.15(80.06%)d 0.03(0.64%)
f 0.00(0.01%)

0.087% N 8 s(45.48%)p 1.16(52.85%)d 0.04(1.63%)
f 0.00(0.04%)

0.054% C 9 s(18.34%)p 4.40(80.67%)d 0.05(0.94%)
f 0.00(0.06%)

0.149% N 10 s(57.22%)p 0.71(40.75%)d 0.03(1.99%)
f 0.00(0.04%)

0.061% C 13 s(35.16%)p 1.81(63.78%)d 0.02(0.79%)
f 0.01(0.27%)

0.042% C 18 s(28.43%)p 2.43(69.00%)d 0.08(2.35%)
f 0.01(0.22%)

0.082% C 19 s(23.92%)p 3.11(74.49%)d 0.06(1.53%)
f 0.00(0.06%)

0.012% C 20 s(42.39%)p 1.23(51.98%)d 0.13(5.34%)
f 0.01(0.29%)

0.041% C 28 s(30.45%)p 2.25(68.65%)d 0.03(0.87%)
f 0.00(0.03%)

0.016% C 29 s(50.53%)p 0.88(44.26%)d 0.10(5.15%)
f 0.00(0.06%)

0.017% C 32 s(26.61%)p 2.62(69.78%)d 0.12(3.13%)

		f 0.02(0.48%)
1.289%	C 33 s(13.68%)p	6.27(85.79%)d 0.04(0.53%)
		f 0.00(0.00%)
0.024%	H 34 s(97.64%)p	0.02(2.36%)
0.022%	H 35 s(97.86%)p	0.02(2.14%)
0.189%	H 36 s(99.58%)p	0.00(0.42%)
0.026%	C 41 s(43.59%)p	1.25(54.31%)d 0.05(2.06%)
		f 0.00(0.04%)
0.026%	C 42 s(15.04%)p	5.23(78.69%)d 0.40(6.00%)
		f 0.02(0.27%)
0.013%	C 52 s(29.81%)p	2.16(64.41%)d 0.19(5.71%)
		f 0.00(0.08%)

Table S7. Natural bond indices (NBI) in complex **3**.

	Pt1	**In2**	**C33**	**N7**	**Cl3**	**N6**	**N8**	**N10**
Pt1	-	0.7133	0.8206	0.4612	-	-	-	-
In2	0.7133	-	-	-	0.7608	0.3686	0.4495	0.3819

Table S8. Wiberg bond indices (WBI) in complex **3**.

	Pt1	**In2**	**C33**	**N7**	**Cl3**	**N6**	**N8**	**N10**
Pt1	-	0.5088	0.6735	0.2127	-	-	-	-
In2	0.5088	-	-	-	0.5788	0.1358	0.2020	0.1458

Complex **4**:

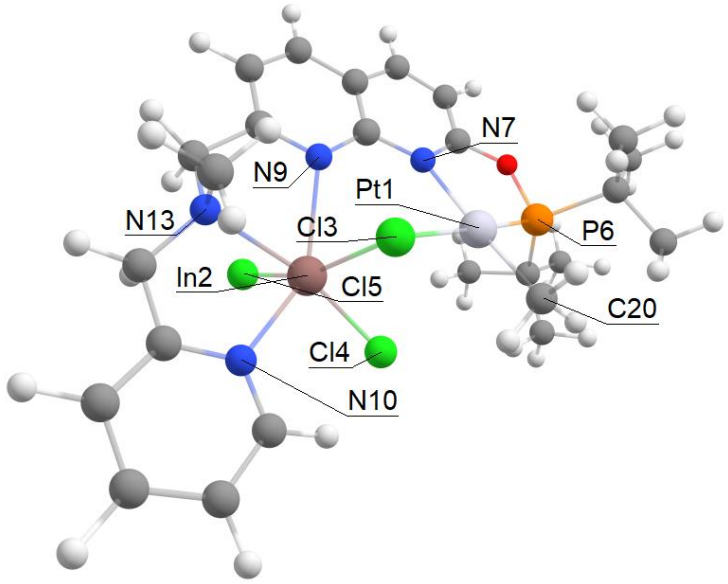

Figure S42. Atom numbering scheme in complex **4** used in NBO analysis.

No significant bonding interactions could be identified between Pt1 and In2.

Table S9. Natural bond indices (NBI) in complex **4**.

	Pt1	**In2**	**Cl3**	**N7**	**C20**	**Cl4**	**Cl5**	**N9**	**N10**	**N13**
Pt1	-	0.1512	0.4953	0.4164	0.8495	-	-	-	-	-
In2	0.1512	-	0.6508	-	-	0.7944	0.7849	0.4521	0.5020	0.4076

Table S10. Wiberg bond indices (WBI) in complex **3**.

	Pt1	**In2**	**Cl3**	**N7**	**C20**	**Cl4**	**Cl5**	**N9**	**N10**	**N13**
Pt1	-	0.0229	0.2453	0.1734	0.7217	-	-	-	-	-
In2	0.0229	-	0.4235	-	-	0.6310	0.6161	0.2044	0.2520	0.1662

The reactivity of a free ligand with In and Ga salts

Coordination of a free ligand with $InCl_3$

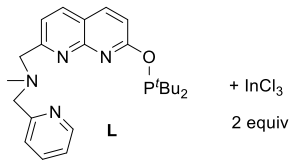

To a solution of a free ligand **L** (8.6 mg, 0.02 mmol) in CD_2Cl_2 (0.5 mL) in a J. Young NMR tube, $InCl_3$ (9.0 mg, 0.04 mmol, 2 equiv) was added, and the reaction was monitored with ^1H NMR spectroscopy, which showed gradual disappearance of the singlets of CH_2 groups characteristic of a free ligand **L** to the appearance of the doublets corresponding to geminal coupling in the CH_2 groups of the ligand and consistent with coordination of the metal to an N-donor site (presumably amine, pyridine and N-atom of naphthyridine adjacent to amine). The single crystals of the product could not be obtained.

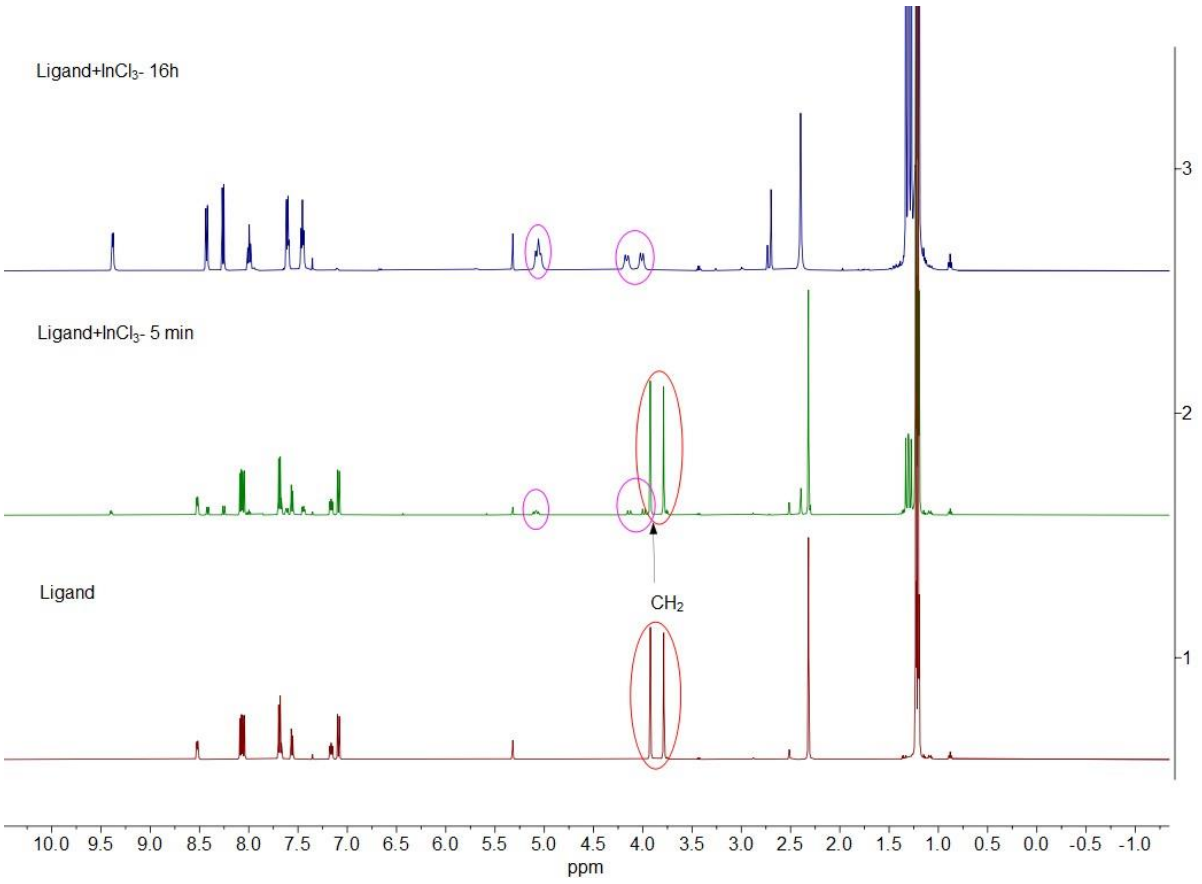

Figure S43. ^1H NMR spectrum of free **L** (bottom) and **L** after treatment with $InCl_3$ for 5 min (green line), after 16 h (purple line) in CD_2Cl_2 at 25 °C.

Coordination of a free ligand with $InCl_2$

To a solution of **L** (8.7 mg, 0.02 mmol) in CD_2Cl_2 (0.5 mL) in a J. Young NMR tube, $InCl_2$ (8.5 mg, 0.04 mmol, 2 equiv) was added, and the reaction was monitored with ^1H NMR spectroscopy. Similarly to the reactivity with $InCl_3$, singlets of CH_2 groups of a free ligand disappeared over time, while a new set of geminally coupled doublets of the CH_2 groups appeared indicative of a metal coordination to N-donor sites at the ligand. The splitting pattern and position of the CH_2 peaks were very similar to those observed during the treatment with $InCl_3$ which could indicate that redox-disproportionation may occur in solutions of $InCl_2$ to In^+ and $InCl_4^-$ as previously reported in the literature (see ref 20 in the main manuscript). The mass spectrometric analysis of the reaction mixture containing a free ligand and $InCl_2$ also confirmed the presence of $InCl_4^-$ anions. The single crystals of the product could not be obtained.

ESI-HRMS (m/z neg): Found (Calcd): $[InCl_4]^-$, $Cl_4{}^{115}In^-$: 254.7851 (254.7797).

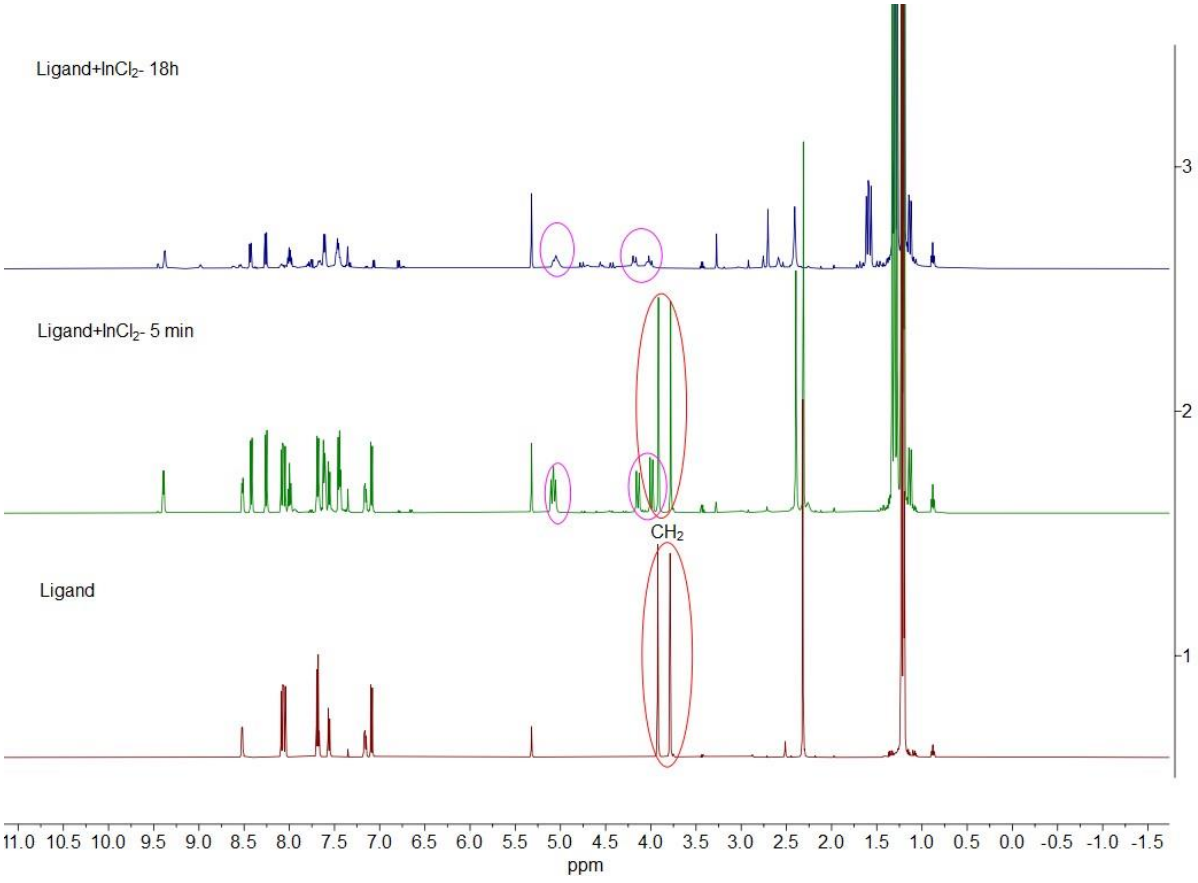

Figure S44. ^1H NMR spectrum of a free **L** (bottom) and **L** after treatment with $InCl_2$ for 5 min (green line), after 18 h (purple line) in CD_2Cl_2 at 25 °C.

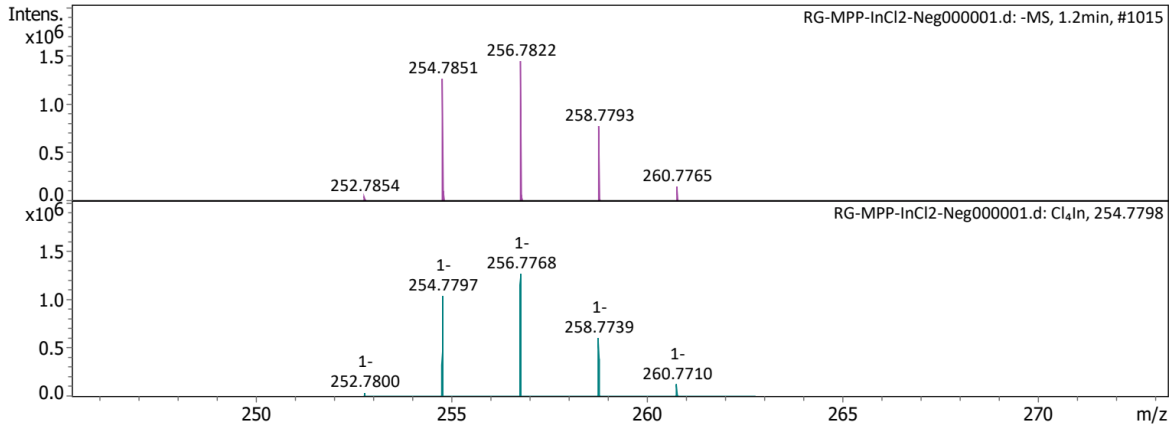

Figure S45. Negative mode ESI-(HR)MS spectrum of an acetonitrile solution of **L+InCl$_2$** (top) and simulated spectrum for $Cl_4{}^{115}In^-$ (bottom).

Attempted reactivity of a free ligand L with $GaCl_3$ and Ga_2Cl_4

When the analogous reactions were performed using 2 equiv of $GaCl_3$ (7.0 mg, 0.04 mmol) and a free ligand **L** (8.5 mg, 0.02 mmol) in CD_2Cl_2 (0.5 mL), the peaks corresponding to a free ligand disappeared already after 5 min at RT, and after 16 h at RT, a mixture of products was formed. Although the reaction was less clean compared to indium salts and a mixture of several components was present, the characteristic doublets of geminally split CH_2 could be recognized indicative of Ga coordination to an N-donor sites at the ligand. The product could not be isolated or purified and eventually undergoes decomposition, presumably phosphite arm splitting.

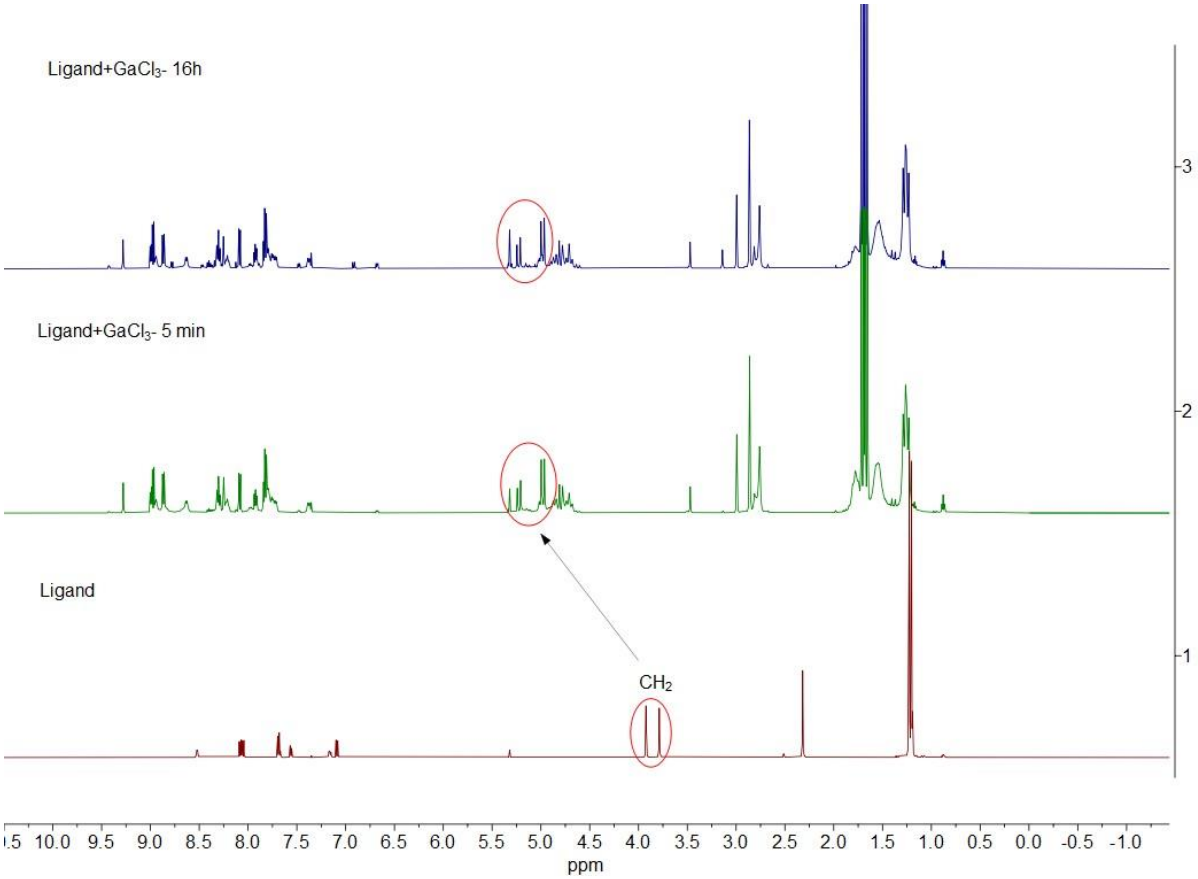

Figure S46. Full ^{1}H NMR spectrum of **L** (bottom) and **L1** after reaction with $GaCl_3$ for 5 min (green line), after 16h (purple line) in CD_2Cl_2 at 25 °C.

Similarly, the treatment of **L** (8.5 mg, 0.02 mmol) with Ga_2Cl_4 (6.0 mg, 0.02 mmol) in THF-d_8 (0.5 mL) produced a mixture of products; however, clear geminal splitting of CH_2 groups could be observed in ^{1}H NMR spectra. Mass spectrometric analysis showed the presence of the $GaCl_4^-$ anion consistent with possible redox disproportionation (see ref 19 in the main manuscript and discussion).

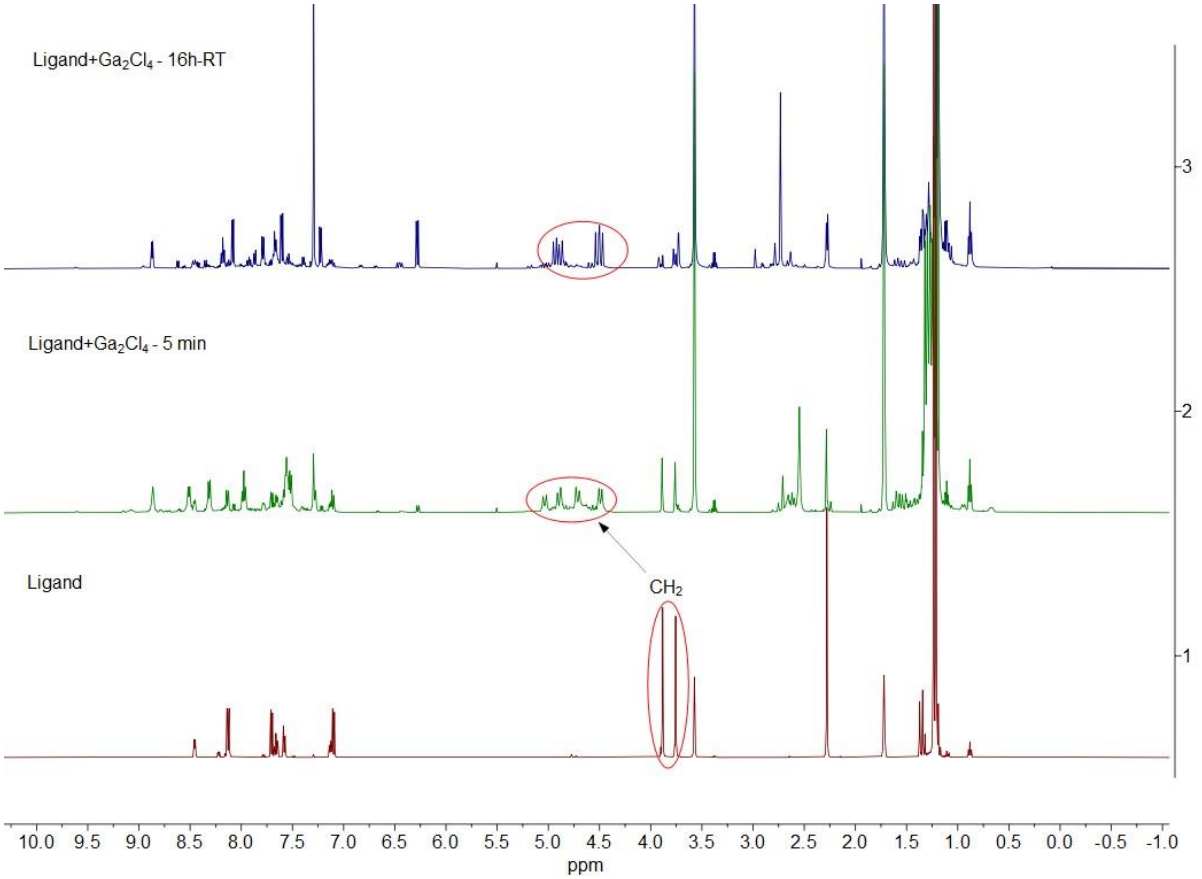

Figure S47. ^{1}H NMR spectrum of a free **L** (bottom) and **L** after treatment with Ga_2Cl_4 for 5 min (green line), after 16 h (purple line) in THF-d_8 at 25 °C.

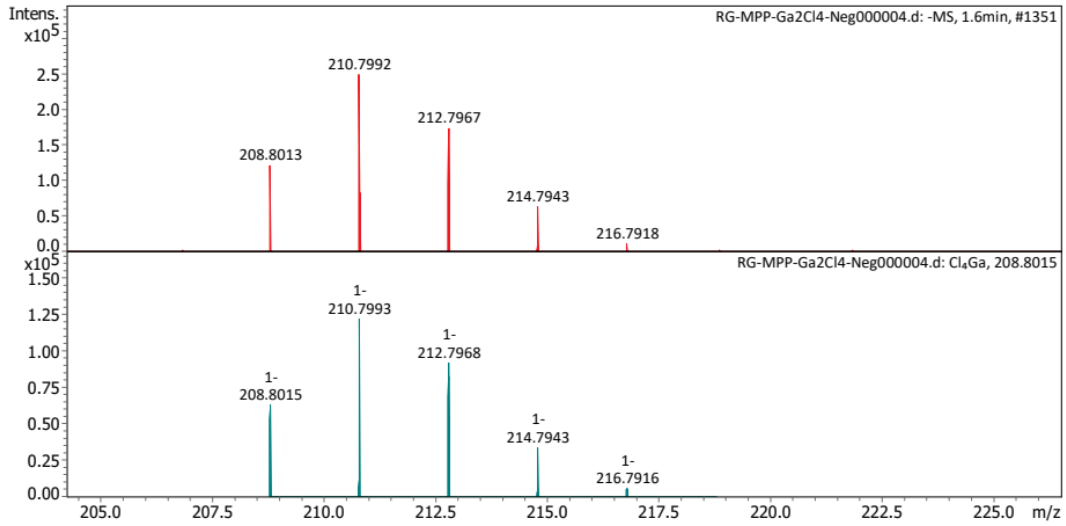

Figure S48. Negative mode ESI-(HR)MS spectrum of an acetonitrile solution of **L+Ga_2Cl_4** (top) and simulated spectrum for $[GaCl_4]^-$ (bottom).

Proposed mechanism of transmetalation

For the mechanistic investigation, the intermediates and transition states were optimized using the ωB97XD functional[3] and def2-tzvp basis set[4] all geometries were optimized in solvent (dichloromethane) using the SMD solvation model.[16] Analytical frequency calculations (at 298.15 K and 1 atm) performed on the resultant geometries conformed to zero imaginary frequencies for all ground states and one imaginary frequency for the transition states. Gibbs free energies are reported as the sum of solvent-corrected electronic and thermal free energies. The IRC calculations were performed to confirm the nature of each transition state. All geometries are provided as XYZ files. Animation corresponding to an imaginary frequency from vibrational analysis is provided as a GIF file. A movie file (GIF) illustrating the intrinsic reaction coordinate (IRC) calculations corresponding to a transition state is also supplied.

The proposed pathway for the transmetalation from $PtMe_2$ to indium salts involves the initial coordination of $InCl_3$ to the vacant N-donor binding site of the ligand in complex **1**. Although no intermediates could be detected by NMR even at short reaction times (see Figures S21, S33), the possibility of $InCl_3$ coordination to an N-donor site was confirmed by NMR spectroscopy when free ligand (in the absence of Pt) was treated with $InCl_3$ (see Figure S43) resulting in CH_2 geminal splitting indicative of a metal coordination to an N-donor chelate site of the ligand (tertiary amine, pyridyl of picolyl arm, and N-atom of naphthyridine adjacent to an amine arm). As described above (Figure S44), the treatment of a free ligand with $InCl_2$ resulted in a similar set of NMR signals suggesting that coordination of $InCl_2$ could be accompanied by its redox disproportionation to In^{I} and In^{III} (see ref 20 in the main manuscript); thus, similar mechanism could be involved in the formation of $InMeCl_3^-$ when complex **1** was treated with $InCl_2$.

The computational analysis showed that while no transition state could be found starting from $InCl_3$ adduct **A-In** with all three N-donors coordinated to In, the isomer **B-In** formed by dissociation of the pyridine from In is accessible. From intermediate **B-In**, a transition state **TS-In** was found leading to the Me group transfer to $PtMe_2$ fragment to In and the formation of intermediate **C-In** where one of the chlorines at $InMeCl_3^-$ is bridging between In and Pt (Figure S49). Extrusion of an anionic $InMeCl_3^-$ would lead to the formation of a coordinatively unsaturated complex **D** (which could be partially stabilized by a weak interaction with a remote picolyl arm or other donors), which can be further stabilized by coordination to another equivalent of $InCl_3$ to give a final product **4**.

In the case of treatment with $InCl_2$, product **3** could result from the stabilization of **D** by coordination of $In^{I}Cl$ in the final product resulting from redox disproportionation of $InCl_2$ (see ref 20 in the main manuscript and discussion).

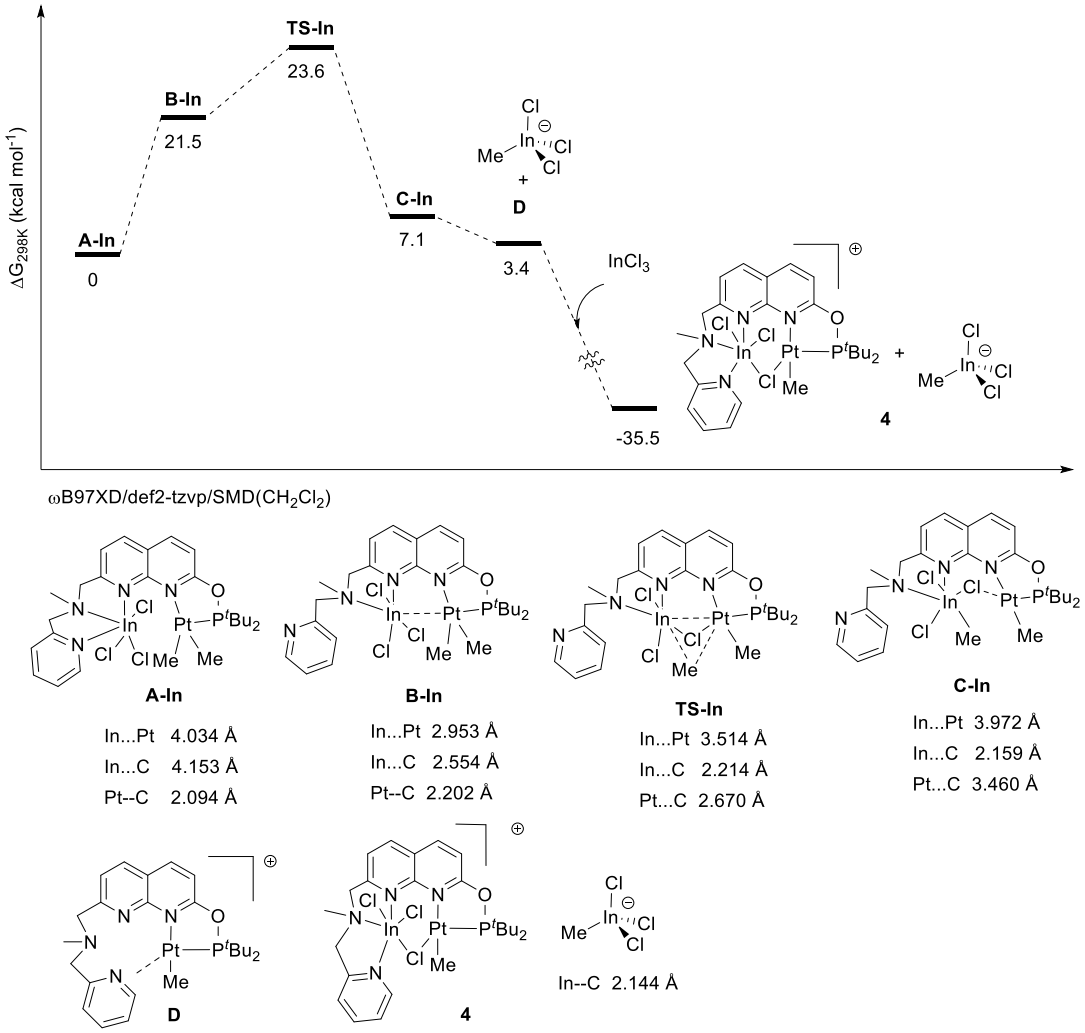

Figure S49. Gibbs free energy profile for the transmetalation to form **4** and selected interatomic distances in geometry-optimized structures.

Extensive search for the transmetalation pathway in possible cationic intermediates (e.g. $[(\mathbf{L})InCl_{2\cdots}PtMe_2]^{+}[InCl_4]^{-}$ was also performed, but no transitions states could be located during this study.

The reactivity with Ga_2Cl_4 could follow a similar pathway via initial coordination of $GaCl_3$ to an N-donors of the ligand followed by Pt-Me group transfer and stabilization of the product by coordination to formally $Ga^{I}Cl$. Detailed mechanistic comparison between In and Ga will be a subject of a future investigation.

Table S11. Free energy profile for transmetalation from Pt to $InCl_3$ to form **4**.

Speciation	ΔG (Hartree)			Sum of ΔG (Hartree)	Relative ΔG (kcal mol^{-1})
A-In+$InCl_3$	-3339.976536	-1571.040010		-4911.016546	0.0
B-In+$InCl_3$	-3339.976536	-1571.040010		-4910.982222	21.5
TS-In+$InCl_3$	-3339.938944	-1571.040010		-4910.978954	23.6
C-In+$InCl_3$	-3339.965213	-1571.040010		-4911.005223	7.1
D + $InCl_3Me^-$+$InCl_3$	-1728.881427	-1611.089759	-1571.040010	-4911.011196	3.4
[(**L**)$InCl_2$(μ-Cl)$PtMe]^+$ + $InCl_3Me^-$ (Complex **4**)	-3299.983289	-1611.089759		-4911.073048	-35.5

The X-ray structure determination details

The X-ray diffraction data for the single crystals of **2-4** were collected on a Rigaku XtaLab PRO instrument (κ-goniometer) with a PILATUS3 R 200K hybrid pixel array detector using Mo *K*α (0.71073 Å) or Cu *K*α (1.54184 Å) radiation monochromated by means of multilayer optics. The performance mode of MicroMax^{TM}-003 microfocus sealed X-ray tubes was 50 kV, 0.60 mA. The diffractometer was equipped with a Rigaku GN2 system for low temperature experiments. Images were indexed and integrated and data were corrected using the *CrysAlisPro* data reduction package (Rigaku Oxford Diffraction).

The structures were solved by the *intrinsic* phasing approach using *SHELXT*-2018/2 [17] and refined by the full-matrix least-squares on F^2 using *SHELXL*-2018/3.[18] Non-hydrogen atoms were refined anisotropically. The positions of hydrogen atoms of methyl groups were found using rotating group refinement with idealized tetrahedral angles. The other hydrogen atoms were inserted at the calculated positions and refined as riding atoms. Disorder, if present, was resolved using free variables and reasonable restraints on geometry and anisotropic displacement parameters.

Crystallographic data for 2.

$C_{26.90}H_{40.71}Cl_{6.10}Ga_2N_4OPPt$ ($C_{25}H_{36}ClGaN_4OPPt$, $C_{0.9}H_{2.71}Cl_{3.1}Ga$, CH_2Cl_2), yellow needle (0.122 × 0.006 × 0.005 mm^3), formula weight 1017.77 g mol^{-1}; triclinic, $P\bar{1}$ (No. 2), a = 8.30726(14) Å, b = 15.06540(19) Å, c = 15.9963(2) Å, α = 70.9877(12)°, β = 84.8936(13)°, γ = 79.8892(12)°, V = 1862.28(5) Å^3, Z = 2, Z' = 1, T = 100(2) K, d_{calc} = 1.815 g cm^{-3}, μ(Cu *K*α) = 13.224 mm^{-1}, F(000) = 994; T_{max}/T_{min} = 0.8249/0.8196; 57844 reflections were collected (2.924° ≤ θ ≤ 72.397°, index ranges: –9 ≤ h ≤ 10, –18 ≤ k ≤ 18, and –19 ≤ l ≤ 19), 7196 of which were unique, R_{int} = 0.0690, $R_σ$ = 0.0309; completeness to θ of 72.397° 97.7 %. The refinement of 427 parameters with 212 restraints converged to $R1$ = 0.0347 and $wR2$ = 0.0927 for 6645 reflections with $I > 2σ(I)$ and $R1$ = 0.0375 and $wR2$ = 0.0945 for all data with goodness-of-fit S = 1.089 and residual electron density $ρ_{max}/ρ_{min}$ = 1.203/–1.722 e Å^{-3}, rms 0.132 e Å^{-3}; max shift/e.s.d. in the last cycle 0.001.

Crystallographic data for 3.

$C_{27}H_{41}Cl_6In_2N_4OPPt$ ($C_{25}H_{36}ClInN_4OPPt$, CH_3Cl_3In, CH_2Cl_2), dark yellow plate (0.152 × 0.057 × 0.016 mm^3), formula weight 1106.04 g mol^{-1}; monoclinic, $P2_1/n$ (No. 14), a = 8.88651(18) Å, b = 12.2296(2) Å, c = 35.1991(6) Å, β = 93.5845(18)°, V = 3817.89(13) Å^3, Z = 4, Z' = 1, T = 100(2) K, d_{calc} = 1.924 g cm^{-3}, μ(Mo *K*α) = 5.342 mm^{-1}, F(000) = 2128; T_{max}/T_{min} = 1.000/0.631; 39366 reflections were collected (2.793° ≤ θ ≤ 28.728°, index ranges: –11 ≤ h ≤ 11, –16 ≤ k ≤ 13, and –39 ≤ l ≤ 47), 9748 of which were unique, R_{int} = 0.0713, $R_σ$ = 0.0657; completeness to θ of 28.728° 98.6 %. The refinement of 398 parameters with 41 restraints converged to $R1$ = 0.0560 and $wR2$ = 0.1126 for 8077 reflections with $I > 2σ(I)$ and

$R1$ = 0.0706 and $wR2$ = 0.1165 for all data with goodness-of-fit S = 1.130 and residual electron density ρ_{max}/ρ_{min} = 3.522/–2.384 e Å^{-3}, rms 0.215 e Å^{-3}; max shift/e.s.d. in the last cycle 0.001.

Crystallographic data for 4.

$C_{28.77}H_{41.30}Cl_{6.23}In_2N_4OPPt$ ($C_{25}H_{36}Cl_3InN_4OPPt$, $C_{0.77}H_{2.3}Cl_{3.23}In$, 0.5($C_6H_6$)), yellow plate (0.187 × 0.035 × 0.014 mm^3), formula weight 1135.93 g mol^{-1}; triclinic, $P\bar{1}$ (No. 2), a = 8.71612(17) Å, b = 14.4778(2) Å, c = 17.6581(4) Å, α = 65.9038(18)°, β = 81.2608(16)°, γ = 73.8299(16)°, V = 1951.78(7) Å^3, Z = 2, Z' = 1, T = 100(2) K, d_{calc} = 1.933 g cm^{-3}, μ(Mo Kα) = 5.243 mm^{-1}, F(000) = 1094; T_{max}/T_{min} = 1.000/0.392; 78879 reflections were collected (2.435° ≤ θ ≤ 33.779°, index ranges: –13 ≤ h ≤ 13, –22 ≤ k ≤ 22, and –27 ≤ l ≤ 27), 14923 of which were unique, R_{int} = 0.0451, $R_σ$ = 0.0372; completeness to θ of 33.779° 95.3 %. The refinement of 404 parameters with 2 restraints converged to $R1$ = 0.0297 and $wR2$ = 0.0640 for 12710 reflections with $I > 2σ(I)$ and $R1$ = 0.0401 and $wR2$ = 0.0669 for all data with goodness-of-fit S = 1.038 and residual electron density ρ_{max}/ρ_{min} = 2.476/–1.657 e Å^{-3}, rms 0.144 e Å^{-3}; max shift/e.s.d. in the last cycle 0.003.

Detailed information about crystal structure determination can be accessed via supplementary cif files. Deposition numbers CCDC 2350091 (for **2**), 2350092 (for **3**), and 2350093 (**4**) contain the supplementary crystallographic data for this paper. These data are provided free of charge by the joint Cambridge Crystallographic Data Centre and Fachinformationszentrum Karlsruhe Access Structures service www.ccdc.cam.ac.uk/structures.

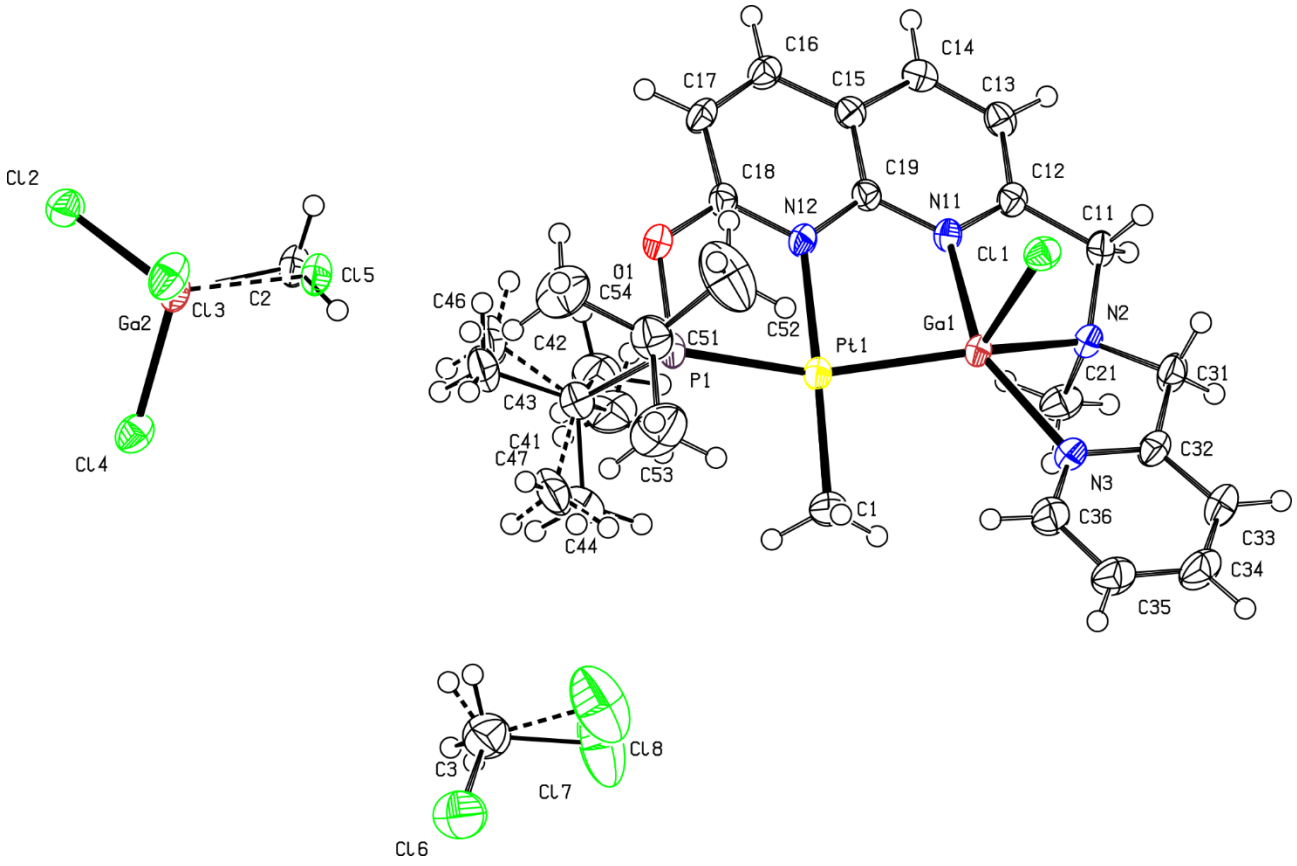

Figure S50. ORTEP at 50 % probability level of anisotropic displacement ellipsoids of non-hydrogen atoms for compound **2** according to SC-XRD data. Selected interatomic distances [Å]: Pt1–Ga1 2.4239(5), Pt1–P1 2.2649(10), Pt1–N12 2.120(3), Pt1–C1 2.076(5), Ga1–Cl1 2.2898(11), Ga1–N11 2.227(3), Ga1–N2 2.189(3), Ga1–N3 2.150(3).

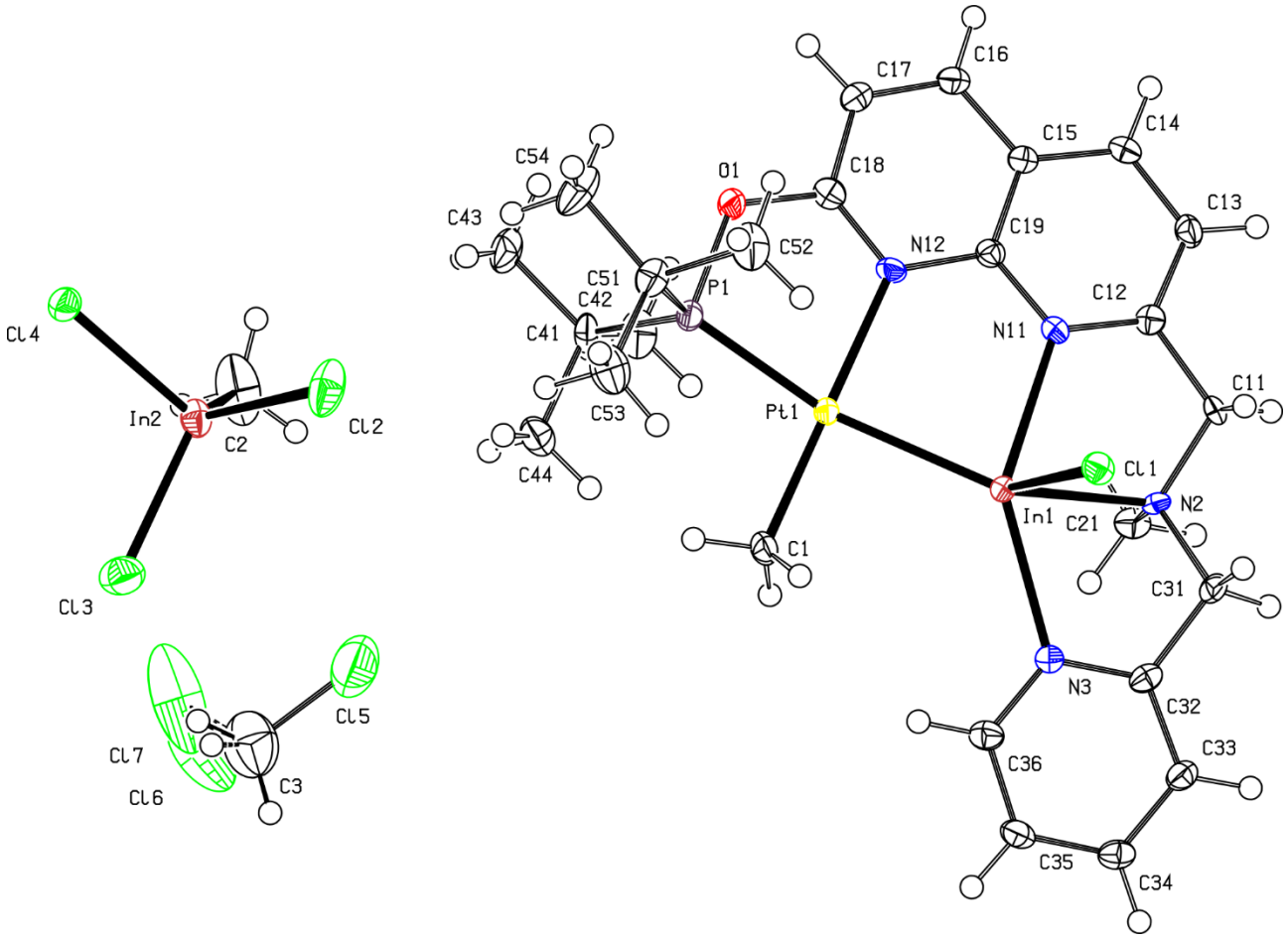

Figure S51. ORTEP at 50 % probability level of anisotropic displacement ellipsoids of non-hydrogen atoms for compound **3** according to SC-XRD data. Selected interatomic distances [Å]: Pt1–In1 2.5794(5), Pt1–P1 2.2374(16), Pt1–N12 2.169(5), Pt1–C1 2.076(7), In1–Cl1 2.4679(17), In1–N11 2.435(5), In1–N3 2.361(5), In1–N2 2.380(5).

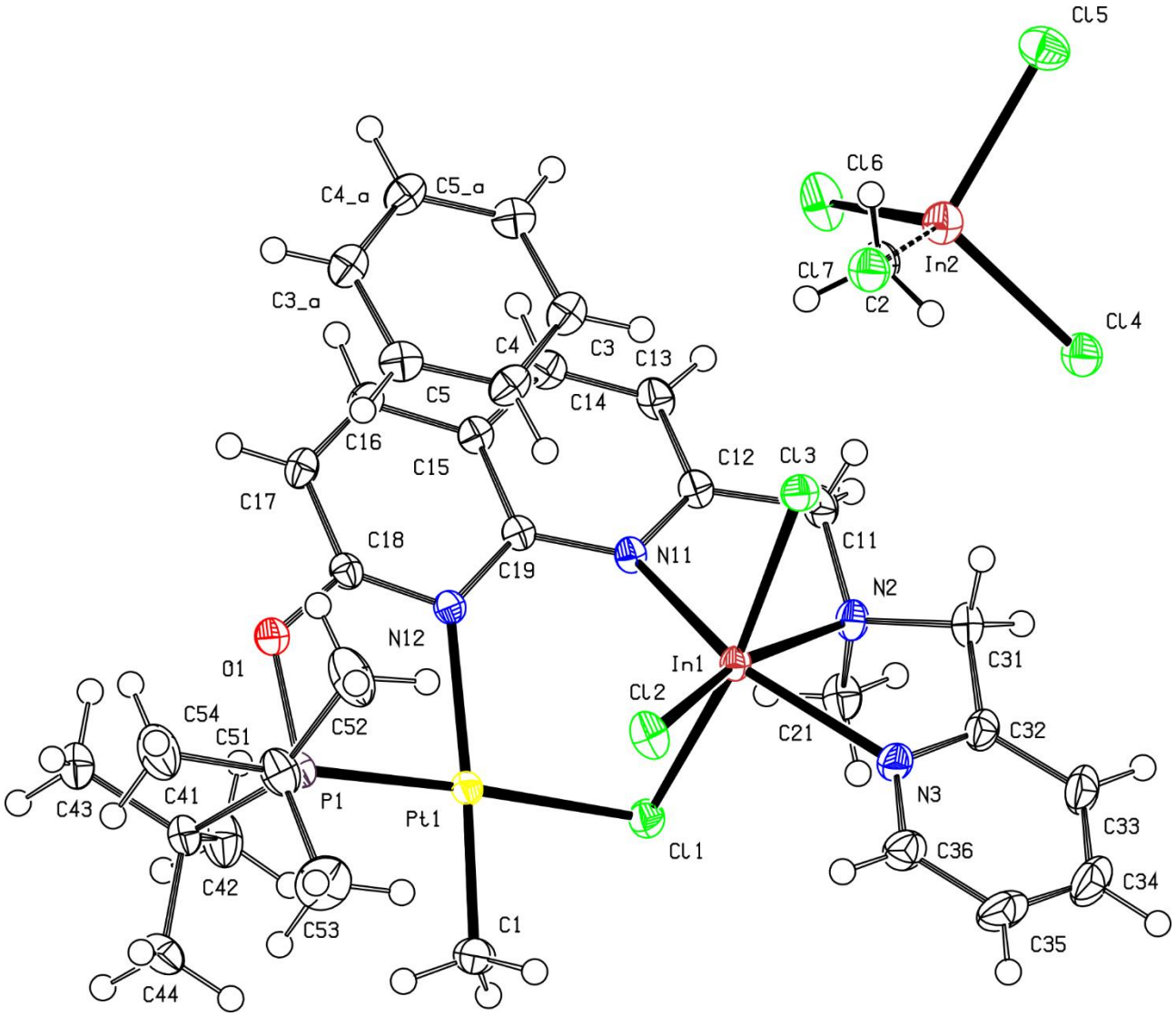

Figure S52. ORTEP at 50 % probability level of anisotropic displacement ellipsoids of non-hydrogen atoms for compound **4** according to SC-XRD data. Selected interatomic distances [Å]: Pt1–Cl1 2.4133(6), Pt1–P1 2.1623(6), Pt1–N12 2.2219(19), Pt1–C1 2.049(3), In1–Cl1 2.5450(6), In1–Cl2 2.4054(6), In1–Cl3 2.4331(6), In1–N11 2.3342(19), In1–N2 2.325(2), In1–N3 2.274(2).

References

1. S. Deolka, O. Rivada, S. L. Aristizábal, R. R. Fayzullin, S. Pal, K. Nozaki, E. Khaskin and J. R. Khusnutdinova, *Chem. Sci.*, 2020, **11**, 5494-5502.
2. Gaussian 16, Revision C.01, M. J. Frisch, G. W. Trucks, H. B. Schlegel, G. E. Scuseria, M. A. Robb, J. R. Cheeseman, G. Scalmani, V. Barone, G. A. Petersson, H. Nakatsuji, X. Li, M. Caricato, A. V. Marenich, J. Bloino, B. G. Janesko, R. Gomperts, B. Mennucci, H. P. Hratchian, J. V. Ortiz, A. F. Izmaylov, J. L. Sonnenberg, D. Williams-Young, F. Ding, F. Lipparini, F. Egidi, J. Goings, B. Peng, A. Petrone, T. Henderson, D. Ranasinghe, V. G. Zakrzewski, J. Gao, N. Rega, G. Zheng, W. Liang, M. Hada, M. Ehara, K. Toyota, R. Fukuda, J. Hasegawa, M. Ishida, T. Nakajima, Y. Honda, O. Kitao, H. Nakai, T. Vreven, K. Throssell, J. A. Montgomery, Jr., J. E. Peralta, F. Ogliaro, M. J. Bearpark, J. J. Heyd, E. N. Brothers, K. N. Kudin, V. N. Staroverov, T. A. Keith, R. Kobayashi, J. Normand, K. Raghavachari, A. P. Rendell, J. C. Burant, S. S. Iyengar, J. Tomasi, M. Cossi, J. M. Millam, M. Klene, C. Adamo, R. Cammi, J. W. Ochterski, R. L. Martin, K. Morokuma, O. Farkas, J. B. Foresman, and D. J. Fox, Gaussian, Inc., Wallingford CT, 2019.
3. J.-D. Chai and M. Head-Gordon, *PCCP*, 2008, **10**, 6615-6620.
4. F. Weigend and R. Ahlrichs, *PCCP*, 2005, **7**, 3297-3305.
5. AIMAll (Version 19.10.12), Todd A. Keith, TK Gristmill Software, Overland Park KS, USA, 2019 (aim.tkgristmill.com).
6. R. F. W. Bader, *Chem. Rev.*, 1991, **91**, 893-928.
7. C. Lepetit, P. Fau, K. Fajerwerg, M. L. Kahn and B. Silvi, *Coord. Chem. Rev.*, 2017, **345**, 150-181.
8. R. Bianchi, G. Gervasio and D. Marabello, *Inorg. Chem.*, 2000, **39**, 2360-2366.
9. P. R. Varadwaj, A. Varadwaj and H. M. Marques, *J. Phys. Chem. A*, 2011, **115**, 5592-5601.
10. a) P. R. Varadwaj, I. Cukrowski and H. M. Marques, *J. Phys. Chem. A*, 2008, **112**, 10657-10666; b) P. Macchi, D. M. Proserpio and A. Sironi, *J. Am. Chem. Soc.*, 1998, **120**, 13429-13435; c) G. Gervasio, R. Bianchi and D. Marabello, *Chem. Phys. Lett.*, 2004, **387**, 481-484.
11. a) E. Espinosa, I. Alkorta, J. Elguero and E. Molins, *J. Chem. Phys.*, 2002, **117**, 5529-5542; b) D. Cremer and E. Kraka, *Croat. Chem. Acta*, 1985, **57**, 1259-1281; cR. F. W. Bader and H. Essen, *J. Chem. Phys.*, 1984, **80**, 1943-1960.
12. T. Lu and F. Chen, *J. Comput. Chem.*, 2012, **33**, 580-592.

13. NBO 7.0. E. D. Glendening, J. K. Badenhoop, A. E. Reed, J. E. Carpenter, J. A. Bohmann, C. M. Morales, P. Karafiloglou, C. R. Landis, and F. Weinhold, Theoretical Chemistry Institute, University of Wisconsin, Madison, WI (2018).
14. Chemcraft - graphical software for visualization of quantum chemistry computations. https://www.chemcraftprog.com.
15. a) A. E. Reed and P. v. R. Schleyer, *Inorg. Chem.*, 1988, **27**, 3969-3987; b) A. E. Reed and P. v. R. Schleyer, *J. Am. Chem. Soc.*, 1990, **112**, 1434-1445.
16. A. V. Marenich, C. J. Cramer and D. G. Truhlar, *J. Phys. Chem. B*, 2009, **113**, 6378-6396.
17. G. Sheldrick, *Acta Crystallogr., Sect. A*, 2015, **71**, 3-8.
18. G. Sheldrick, *Acta Crystallogr., Sect. C*, 2015, **71**, 3-8.